Impact of intermittent lead exposure on hominid brain evolution

Renaud Joannes-Boyau, Janaina Sena de Souza, Manish Arora, Christine Austin, Kira Westaway, Ian Moffat, Wei Wang, Wei Liao, Yingqi Zhang, Justin Adams, et al.

▶ **To cite this version:**

Renaud Joannes-Boyau, Janaina Sena de Souza, Manish Arora, Christine Austin, Kira Westaway, et al.. Impact of intermittent lead exposure on hominid brain evolution. Science Advances , 2025, 11 (42), ⟨10.1126/sciadv.adr1524⟩. ⟨hal-05390756⟩

HAL Id: hal-05390756

https://hal.science/hal-05390756v1

Submitted on 1 Dec 2025

HAL is a multi-disciplinary open access archive for the deposit and dissemination of scientific research documents, whether they are published or not. The documents may come from teaching and research institutions in France or abroad, or from public or private research centers.

L'archive ouverte pluridisciplinaire **HAL**, est destinée au dépôt et à la diffusion de documents scientifiques de niveau recherche, publiés ou non, émanant des établissements d'enseignement et de recherche français ou étrangers, des laboratoires publics ou privés.

Distributed under a Creative Commons CC BY-NC 4.0 - Attribution - Non-commercial use - International License

Check for updates

ANTHROPOLOGY

Impact of intermittent lead exposure on hominid brain evolution

Renaud Joannes-Boyau[1,2,3]*†, Janaina Sena de Souza[4]†, Manish Arora[5]*†, Christine Austin[5]†, Kira Westaway[6], Ian Moffat[7,8], Wei Wang[9], Wei Liao[9], Yingqi Zhang[3], Justin W. Adams[10,11,2], Luca Fiorenza[10], Flora Dérognat[1], Marie-Helene Moncel[12], Gary T. Schwartz[13], Marian Bailey[1], Filipe F. dos Santos[14,15], Gabriela D. A. Guardia[14], Rafael L. V. Mercuri[14,16], Pedro A. F. Galante[14], Aline M. A. Martins[17,18], Blake L. Tsu[19], Christopher A. Barnes[19], John Yates III[18], Luiz Pedro Petroski[20], Sandra M. Sanchez-Sanchez[4], Jose Oviedo[21], Roberto H. Herai[20], Bernardo Lemos[21,22], Matthew Tonge[1], Alysson R. Muotri[4,17,23]*

Copyright © 2025 The Authors, some rights reserved; exclusive licensee American Association for the Advancement of Science. No claim to original U.S. Government Works. Distributed under a Creative Commons Attribution NonCommercial License 4.0 (CC BY-NC).

Gene-environmental interactions shape the evolution of brain architecture and function. Neuro-oncological ventral antigen 1 (*NOVA1*) is one gene that distinguishes modern humans from extinct hominids. However, the evolutionary pressures that selected the modern *NOVA1* allele remain elusive. Here, we show using fossil teeth that several hominids (*Australopithecus africanus*, *Paranthropus robustus*, early *Homo* sp., *Gigantopithecus blacki*, *Pongo* sp., *Homo neanderthalensis*, and *Homo sapiens*) were consistently exposed to lead over 2 million years, contradicting the idea that lead exposure is solely a modern phenomenon. Moreover, lead exposure on human brain organoids carrying the archaic *NOVA1* variant disrupts *FOXP2* expression in cortical and thalamic organoids, a gene crucial for the development of human speech and language abilities. Overall, the fossil, cellular, and molecular data support that lead exposure may have contributed to the impact of social and behavioral functioning during evolution, likely affording modern humans a survival advantage.

INTRODUCTION

Selective pressures from changing environmental conditions left genetic signatures throughout hominid evolution, which may drive modern human vulnerability to the effects of environmental stressors today (*1*). Exposure to toxic chemicals may also contribute to hominin evolution by affecting group behaviors, but limited data are available on this topic. The prevailing paradigm is that lead (Pb) exposure is a modern phenomenon that only emerged with increased anthropogenic lead released into the environment from human activities, such as mining and smelting, beginning in classical antiquity and medieval societies (*2*) and then intensifying markedly during the Industrial Revolution (*3*). Contrary to this hypothesis, we show that lead exposure was not confined to postanthropogenic lead release but was pervasive throughout hominid evolution, extending as far back as 2 million years. Deficits in intelligence, behavior, and emotional performance have been extensively observed in lead-exposed human populations and animal models (*4*, *5*). However, no clear molecular mechanisms linking lead exposure to hominid evolution have been identified, particularly its role in shaping group dynamics, which we address here.

The genomic sequences of Neanderthals and Denisovans—our closest extinct hominin relatives—offer valuable insights into human evolution. Among the 61 unique protein-coding genes distinguishing modern humans (*6*), the neuro-oncological ventral antigen 1 (*NOVA1*) plays a crucial role in early brain development. *NOVA1* is implicated under conditions such as autism and schizophrenia (*7*–*9*). Previous work has shown that the archaic *NOVA1* variant influences alternative splicing, synaptic protein interactions, and neural connectivity when reintroduced into human brain organoids (*6*). Thus, the exclusive *NOVA1* single-nucleotide alteration, which became nearly fixed in modern humans, might have had functional consequences for our species' evolution (*10*). However, the selective

[1]Geoarchaeology and Archaeometry Research Group, Southern Cross University, Military Road, Lismore, NSW 2480, Australia. [2]Palaeo-Research Institute, University of Johannesburg, Auckland Park, Johannesburg 2006, South Africa. [3]Institute of Vertebrate Paleontology and Paleoanthropology, Chinese Academy of Sciences, Beijing 100044, China. [4]Department of Pediatrics and Cellular & Molecular Medicine, School of Medicine, University of California San Diego, La Jolla, CA 92093, USA. [5]Department of Environmental Medicine, Icahn School of Medicine at Mount Sinai, New York, NY 10029, USA. [6]School of Natural Sciences, Faculty of Science and Engineering, Macquarie University, Sydney, NSW 2109, Australia. [7]Archaeology, College of Humanities, Arts and Social Sciences, Flinders University, Adelaide, SA, Australia. [8]McDonald Institute for Archaeological Research, University of Cambridge, Cambridge, UK. [9]Institute of Cultural Heritage, Shandong University, Qingdao 266237 China. [10]Department of Anatomy and Developmental Biology, Biomedicine Discovery Institute, Monash University, Melbourne, VIC 3800 Australia. [11]Department of Geosciences, Museums Victoria, 11 Nicholson St., Carlton, VIC 3053, Australia. [12]Département Hommes et Environnement, Museum National d'Histoire Naturelle, CNRS 7194, Institut de Paléontologie Humaine, 1 rue René Panhard, 75013 Paris, France. [13]Institute of Human Origins, School of Human Evolution and Social Change, Arizona State University, Tempe, AZ 85287, USA. [14]Hospital Sirio-Libanes, Sao Paulo 01308-060, Brazil. [15]Departamento de Bioquimica, Instituto de Quimica, Universidade de Sao Paulo, Sao Paulo, Brazil. [16]Interunidades em Bioinformática, Universidade de Sao Paulo, Sao Paulo, Brazil. [17]ISSCOR – Integrated Space Stem Cell Orbital Research, Sanford Consortium of Regenerative Medicine, UCSD, La Jolla, CA 92093, USA. [18]Department of Molecular Medicine, The Scripps Research Institute, La Jolla, CA 92037, USA. [19]NGeneBioAI Inc., 9810 Summers Ridge Rd. #100, San Diego, CA 92121, USA. [20]Pontifícia Universidade Católica do Paraná, School of Medicine and Life Sciences, Graduate Program in Health Sciences (PUCPR/PPGCS), Laboratory of Bioinformatics and Neurogenetics (LaBiN), Curitiba, Paraná 80215-901, Brazil. [21]Department of Pharmacology and Toxicology, R Ken Coit College of Pharmacy, University of Arizona, Tucson, AZ 85721, USA. [22]Program in Molecular and Integrative Physiological Science and Department of Environmental Health, Harvard T. H. Chan School of Public Health, Boston, MA 02115, USA. [23]University of California San Diego, Kavli Institute for Brain and Mind, Center for Academic Research and Training in Anthropogeny (CARTA), Archealization Center (ArchC), La Jolla, CA 92093, USA.
*Corresponding author. Email: muotri@ucsd.edu (A.R.M.); manish.arora@mssm.edu (M.A.); renaud.joannes-boyau@scu.edu.au (R.J.-B.)
†These authors contributed equally to this work.

Downloaded from https://www.science.org on October 19, 2025

evolutionary pressures to select this genetic variant among modern human populations remain unknown.

Here, we combine a large archaeogeochemical study of fossil teeth from Africa, Asia, Oceania, and Europe to study lead exposure over 2 million years. We provide mechanistic information about the impact of lead on *FOXP2*-expressing neurons within human cortical and thalamic brain organoids carrying the archaic/extinct *NOVA1* genetic variant. The gene is crucial for the development of human speech and language abilities and, therefore, a key factor for communication and social interactions. This sheds light on the intricate mechanisms through which genetic variations shape our responses to environmental toxicants, ultimately enhancing our understanding of human evolution.

RESULTS

Lead exposure traced across primate evolution through fossil teeth

Using precise validated laser ablation micro spatial sampling protocols (Fig. 1), we analyzed 51 fossil samples (*Australopithecus africanus*, *Paranthropus robustus*, early *Homo* sp., *Gigantopithecus blacki*, *Pongo* sp., *Papio* sp., *Homo neanderthalensis*, and *Homo sapiens*) from regions in Asia, Africa, and Europe. We found clear signals of episodic lead exposure in 73% of the specimens (71% for hominins *Australopithecus*, *Paranthropus*, and *Homo*) (Fig. 2 and tables S1 and S2). Some of the geologically oldest samples, *G. blacki* estimated to be from the early (~1.8 Ma) and middle Pleistocene (~1 Ma), show repeated events of lead exposure separated by periods of negligible lead uptake (Fig. 2) (*11*). Samples from this genus demonstrated the most frequent acute lead exposures. From six cave sites in China, we analyzed fossils of *Pongo* sp., *G. blacki*, and *H. sapiens* extending from the early (~1.8 Ma) to late Pleistocene (~100 ka) (Figs. 2 and 3 and the Supplementary Materials). Our *Australopithecus* and *Papio angusticeps* samples originated in South Africa (Fig. 3B and the Supplementary Materials), and two *H. neanderthalensis* samples were from the Payre region of France (Fig. 3F and the Supplementary Materials). Previous studies have found that cumulative lead in teeth from prehistoric humans, although highly variable, was generally lower than that in modern humans (*12*). Sediment sampling also indicated that *Homo* species from the Middle Paleolithic inhabited caves with high concentrations of lead and other heavy metals (*13*), but exposure levels or patterns are unknown.

We observed lead bands corresponding to discrete zones of high lead concentrations, following the incremental growth pattern of enamel and dentine protein matrix deposition and mineralization during tooth development (see the Supplementary Materials). While postburial alteration of fossil teeth remains a concern for all chemical analyses, the effects of diagenesis result in a diffused pattern of metal deposition and were not collocated with the Pb or the developmental geometry of enamel or dentine mineralization. While dentine,

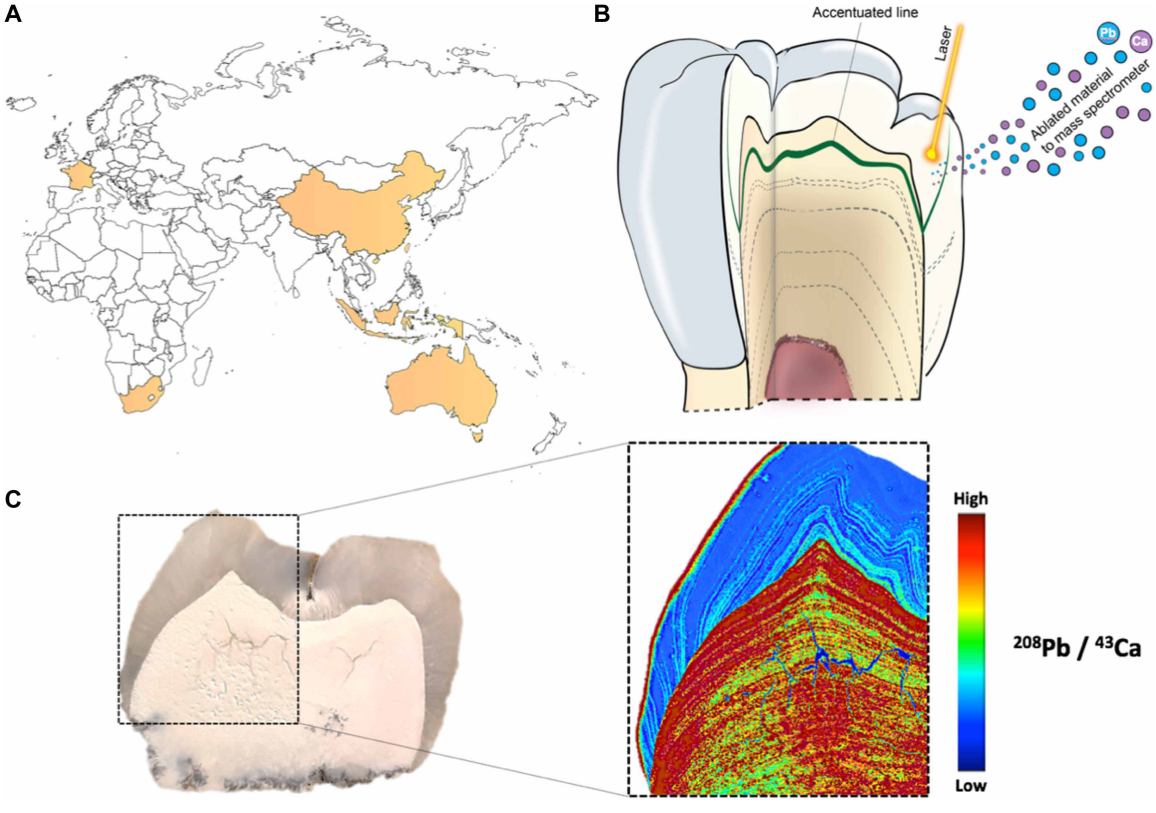

Fig. 1. Reconstructing primate's exposure to environmental lead. (**A**) World map with indication of the country from which the archaeological and modern samples were obtained. (**B**) Sketch of a sectioned fossil tooth analyzed by laser ablation combined with inductively coupled plasma mass spectrometry (LA-ICP-MS). The laser is rastered across the sectioned surface, and ejected material is transported to the mass spectrometer. Green and dashed lines depict the biogenic pattern of metal uptake within growth rings [adapted from (*65*)]. (**C**) Photo (left) of a sectioned *G. blacki* third molar from the site of Queque in China. The $^{208}Pb/^{43}Ca$ distribution from the marked area is shown on the right. The geochemical map reveals a large number of biogenic banding relating to repeated acute exposures to lead.

Downloaded from https://www.science.org on October 19, 2025

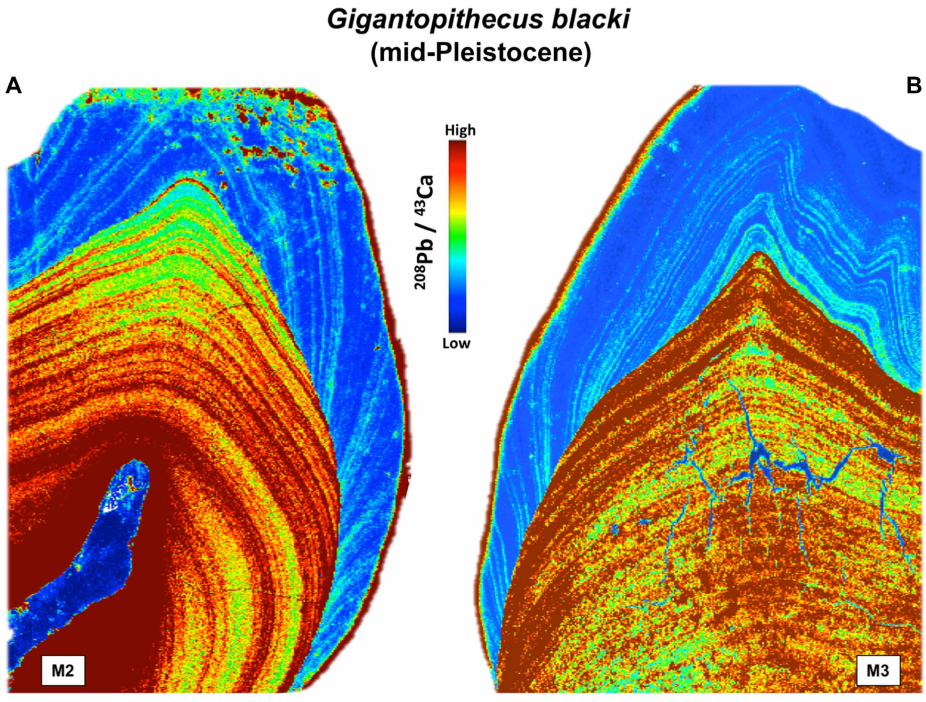

Fig. 2. Lead banding in two *G. blacki* fossil teeth. $^{208}Pb/^{43}Ca$ distribution in second molar (**A**) and third molar (**B**) of *G. blacki* teeth from the site of Queque in Southern China dated to the middle Pleistocene. The Pb banding follows the architecture of the dental tissue growth pattern, which is evidence of its biogenic origin and incorporation during tooth growth. Both teeth show an impressive number of repeated acute exposures to lead.

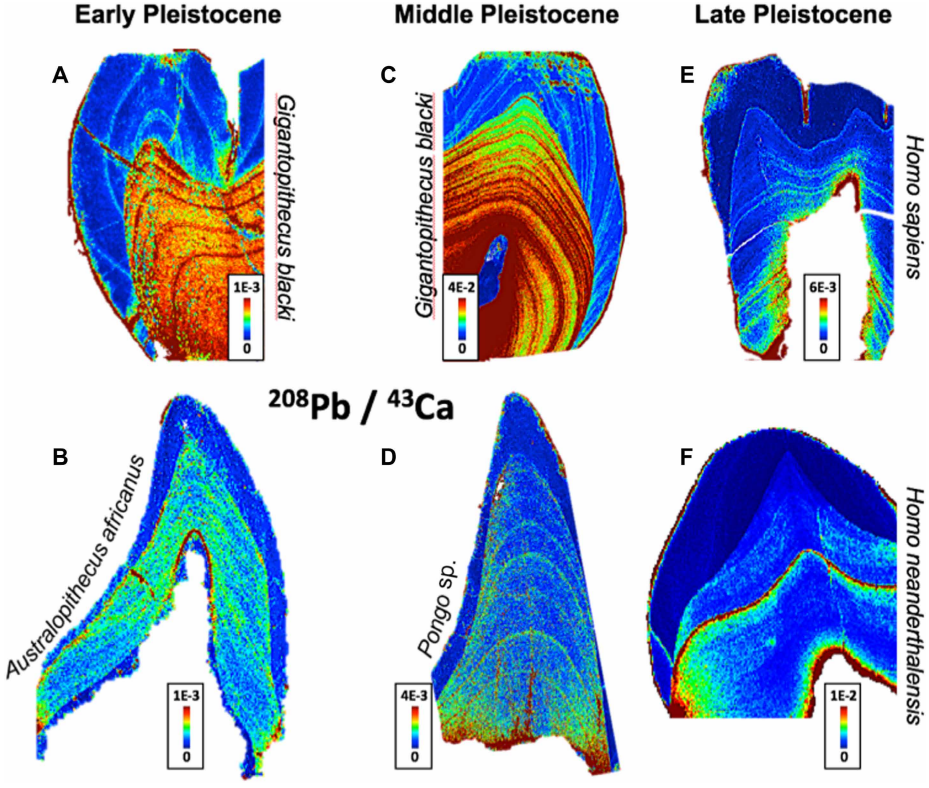

Fig. 3. Lead banding in fossil hominid teeth across the Pleistocene. $^{208}Pb/^{43}Ca$ distribution in (**A**) *G. blacki* third molar from the site of Chuifeng in China. (**B**) *A. africanus* canine from the site of Sterkfontein in South Africa. (**C**) *G. blacki* second molar from the site of Queque in China. (**D**) *Pongo* sp. canine from the site of Shanzu in China. (**E**) *H. sapiens* first molar from the site of Mohui in China. (**F**) *H. neanderthalensis* molar from the site of Payre in France.

Downloaded from https://www.science.org on October 19, 2025

due to its higher organic content and smaller crystal size, is more likely to undergo diagenetic modification than enamel (*14*), several of our samples preserved lead banding in both tissues atypical of diagenesis (Fig. 1). We also measured uranium, a common marker of diagenesis (*15*) in our samples (see the Supplementary Materials). The uranium distribution did not match the lead bands we observed in the analyzed teeth and generally followed a more diffuse pattern with localized "hot spots" (radiated areas) of high uranium concentration in both enamel and dentine tissues, typical of diffusion patterns.

In addition to external environmental sources, it is important to consider that lead can also be released from internal physiological stores. Once lead is absorbed into the body, it is predominantly stored in the skeletal compartment and released during enhanced bone remodeling periods (*16*). High lead release from bones during illness or physiological stresses is recorded in developing teeth as acute lead enrichments such as those observed here (*17*). Cyclical patterns of stress, as measured by enamel defects, have been observed in extant great apes, but it is not clear whether these are associated with seasonal schedules (*18*).

Lead patterns in humans during peak anthropogenic exposure

Evolutionary mismatch occurs when encountering an evolutionary novel environment or an environment that exceeds the range previously experienced in the lineage (*19*), which may have occurred for humans when lead exposure increased substantially and became chronic rather than episodic compared to the exposure patterns recorded during hominid evolution. To compare the lead enrichment patterns we observed in the teeth of extinct hominids with modern postindustrial samples, we analyzed modern human teeth from participants ($n = 12$) born between the 1940s and 1970s in the US when environmental lead exposure from industrial sources, such as leaded automobile fuel and leaded paint, was prevalent and persistent (that is, a chronic continuous exposure) (see the Supplementary Materials). We supplemented this analysis with a human third molar from an individual born in 1994 when lead exposure in the US had reduced substantially.

Our analysis of modern teeth showed lead banding patterns similar to those observed in fossil samples in all but one individual (see the Supplementary Materials). Banding was more prevalent within the crown and became narrower and decreased in intensity toward the root. On the basis of human tooth growth guides (*20*), bands are estimated to occur annually and are broader and of higher intensity during 1 to 6 years of age. This timescale roughly coincides with the late childhood or early juvenile period, a time of rapid bone turnover in humans. Variations in modern children's blood lead have been extensively reported and generally attributed to seasonal variations in lead exposure sources and lead metabolism (via vitamin D) (*21*). Seasonal variations in bone growth velocity and markers of bone remodeling have also been reported (*22*). Therefore, the annual banding of lead in modern human teeth may reflect seasonal variation in external exposure to lead coupled with internal exposure through the release of skeletal stores during bone remodeling. The release of skeletal stores of lead during pregnancy as a result of increased bone resorption is well documented (*16*) and is the main contributor to maternal blood lead (*23*). The release of bone-lead stores has been reported to contribute as much as 90% of blood-lead levels in children when external exposure is relatively low and skeletal lead stores are substantial (*24*).

The higher intensity of lead enrichment banding during 1 to 6 years of age may reflect the higher turnover of bone during this period. Biochemical markers of bone turnover are highest in the first few years after birth, dropping around 2 to 3 years and rising again during the pubertal growth spurt (*25*). However, environmental lead exposure during childhood follows a similar trend, with exposures typically highest during early childhood due to increased hand-to-mouth activity and greater body burden (*26*). Given the complexity of lead kinetics in primate physiology, disentanglement of external and internal lead exposure was impossible in this study. Still, it is clear from our data that lead exposure was not just a postindustrial phenomenon. Furthermore, the presence of lead bands in modern human teeth also supports the inference that the patterns in our fossil teeth are not due to diagenesis. We found similar lead banding patterns in teeth from modern *Papio ursinus* (see the Supplementary Materials) and *Pongo abelii* (see the Supplementary Materials).

The impact of lead on human neurodevelopment

Lead exposure in human neural progenitor cells alters gene expression and primarily affects the *NOVA1*-regulated splicing network, affecting cell proliferation, neuronal differentiation, and axon guidance pathways (*27*). Considering that lead is widespread in nature, causes cognitive alterations in humans, and was detected in archaeological samples and that *NOVA1* is the master regulator of lead-induced alternative splicing, we measured the molecular and cellular impact of lead in brain organoids carrying the modern ($NOVA1^{hu/hu}$) or archaic ($NOVA1^{ar/ar}$) versions of the human *NOVA1* gene.

We previously generated isogenic induced pluripotent stem cells (iPSCs) carrying $NOVA1^{hu/hu}$ or $NOVA1^{ar/ar}$ genetic variants using genome editing in two distinct genetic backgrounds (*6*, *28*). A careful off-target analysis excluded potential problematic clones with undesirable genomic alterations (*6*, *28*). We confirmed the genotype of our cells using target-genome sequencing (fig. S11, A and B). Next, we generate brain cortical organoids (COs) using a semiguided protocol (Fig. 4, A and B, and fig. S11C) (*6*, *29*–*33*). At 2 months, these COs presented $FOXG1^+$, $MAP2^+$, and $SOX2^+$ cell populations (Fig. 4C and fig. S11D). When the COs were at 45 days, they were treated for 10 days with lead acetate (10 and 30 μM) (*27*). After treatment, the medium was changed to one without lead acetate, and the COs were collected after 5 days (at 60 days old). We found that lead treatment did not reduce the organoid diameter in either genetic background (fig. S11, E and F). We also ran a cell cycle profile assay in dissociated COs. We showed that lead treatment decreased the percentage of cells in the G_0-G_1 stage in the $NOVA1^{ar/ar}$ 10 and 30 μM compared to control (CTL) COs (Fig. 4D and fig. S11G).

RNA sequencing identifies gene expression changes from lead exposure

Bulk RNA sequencing (RNA-seq) analyses were performed on mature COs derived from $NOVA1^{hu/hu}$ and $NOVA1^{ar/ar}$ to elucidate the changes induced by lead exposure, which differentially affected genes in these two genetic backgrounds. First, we compared $NOVA1^{hu/hu}$ versus $NOVA1^{ar/ar}$ without any treatment and showed that hundreds of genes were altered [429 down-regulated and 616 up-regulated; false discovery rate (FDR) < 0.05; Fig. 4E and table S3]. Functional enrichment analysis on the top differentially up- and down-regulated genes revealed the top 20 enriched Gene Ontology (GO) pathways, these genes were related to cell motility, neurodevelopment,

Downloaded from https://www.science.org on October 19, 2025

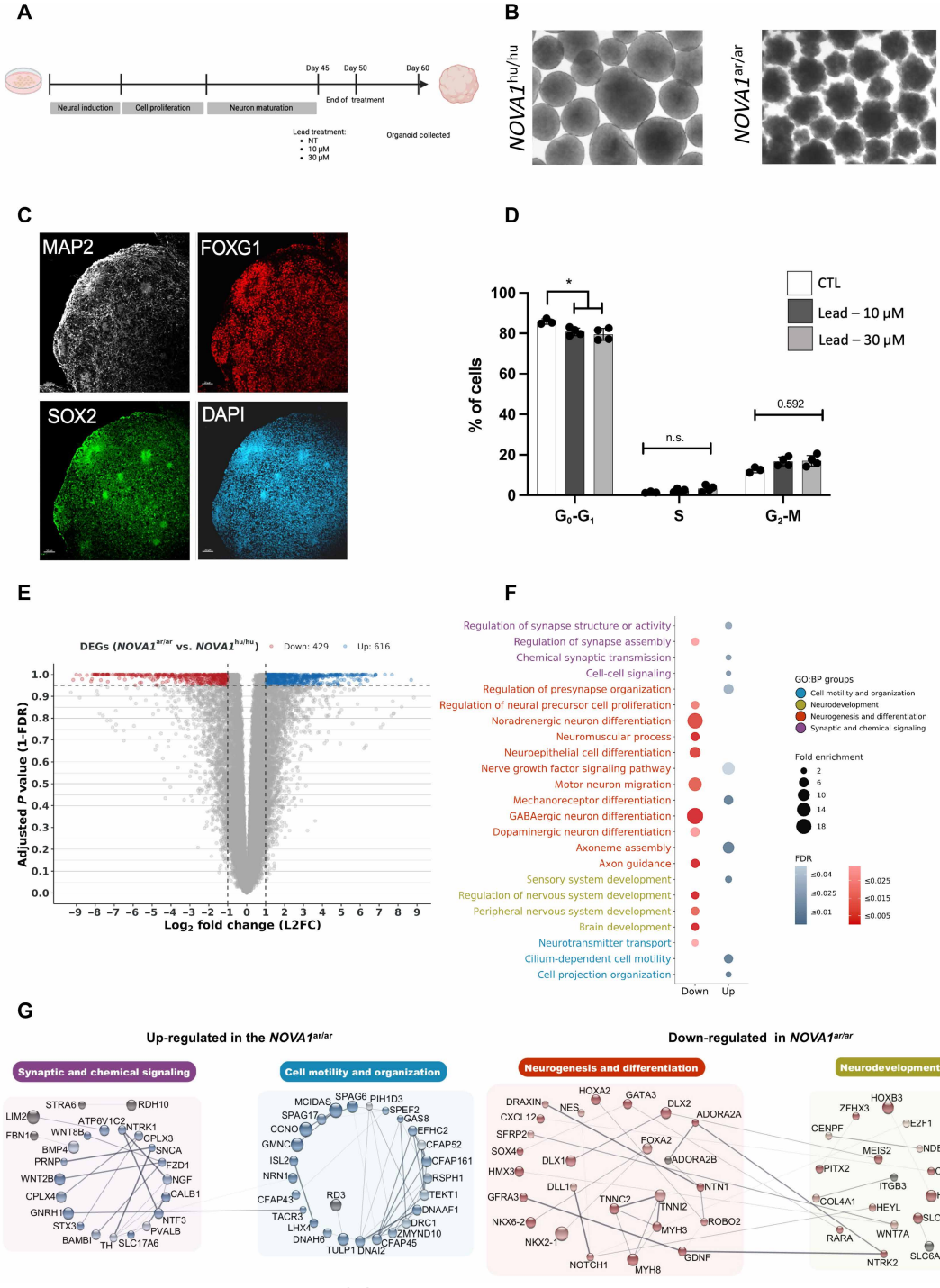

Fig. 4. Characterization of cortical brain organoids of *NOVA1*$^{hu/hu}$ and *NOVA1*$^{ar/ar}$. (**A**) Schematic representation of the brain cortical organoid (COs) differentiation protocol. (**B**) Representative bright-field images of human COs captured at day 16, proliferative stage of neuroprogenitor cells (*NOVA1*$^{hu/hu}$ and *NOVA1*$^{ar/ar}$). (**C**) Representative immunohistochemistry images of 60-day-old brain organoids (*NOVA1*$^{hu/hu}$). COs contain proliferative regions (SOX2^{+}), expressing the cortical marker (FOXG1^{+}) surrounded by mature neurons (MAP2^{+}). Scale bars, 50 µm. (**D**) Cell cycle quantification of brain organoids carrying the *NOVA1*$^{ar/ar}$ genetic variant. CTL, control group. $n \geq 2$. One-way analysis of variance (ANOVA) Tukey test and Kruskal-Wallis test, followed by Dunn's test. n.s., not significant. $^{*}P < 0.05$. (**E**) Volcano plot showing the 616 up-regulated (blue) and 429 down-regulated (red) genes under the *NOVA1*$^{ar/ar}$ condition compared to the *NOVA1*$^{hu/hu}$ control after applying the false discovery rate (FDR) < 0.05 and $\log_2$ fold change (|L2FC|) > 1 filters. (**F**) Bubble plot showing the top enriched Gene Ontology Biological Process (GO:BP) terms (FDR < 0.05; bigger bubbles mean more enrichment) for both the up-regulated (blue) and down-regulated (red) genes shown in (E). Terms are further organized into major color-coded functional "groups." (**G**) Protein-protein interactions (PPIs) showing the differentially expressed genes (DEGs) that represent the major color-coded functional groups shown in (F). Higher STRINGdb scores (minimum cutoff: 0.7, "high confidence") mean less transparency and thicker edges. Higher |L2FC| values mean bigger nodes, while lower FDR values mean darker (blue: up-regulated; red: down-regulated) nodes.

Downloaded from https://www.science.org on October 19, 2025

neurogenesis, neurodifferentiation, and synaptic and chemical signaling (Fig. 4, F and G, and table S4).

Next, we compare the nontreated organoids with the ones exposed to lead. *NOVA1*$^{hu/hu}$ organoids exposed to 10 μM lead presented different groups of down- and up-regulated genes (FDR < 0.05). Functional enrichment analysis on the top differentially up- and down-regulated genes revealed the top 20 enriched pathways, such as cell activation, regulation, and communication of the nervous system, neurodevelopment, and synapses, among others (Fig. 5A; fig. S12, A, B, and E; and tables S4 and S5). *NOVA1*$^{hu/hu}$ COs exposed to 30 μM lead also presented a group of down- and up-regulated genes (FDR < 0.05). Functional enrichment analysis on the top differentially up- and down-regulated genes revealed the top 20 enriched pathways, such as genes related to myelination, axon guidance, neurodevelopment, behavior, synapse, and neuronal processes (Fig. 5B; fig. S12, C, D, and F; and tables S4 and S6). *NOVA1*$^{ar/ar}$ exposed to 10 μM lead presented a group of down- and up-regulated genes (FDR < 0.05). Functional enrichment analysis on the top differentially up- and down-regulated genes revealed the top 20 enriched pathways, such as those related to learning, memory, cognitive functions, neurodevelopment, glial activation, cell fate, and synaptic signaling (Fig. 5, C and E; fig. S13, A and B; and tables S4 and S7).

NOVA1$^{ar/ar}$ exposed to 30 μM lead also presented a group of down- and up-regulated genes (FDR < 0.05). Functional enrichment analysis on the top differentially up- and down-regulated genes revealed the top 20 enriched pathways, such as cell adhesion, motility, morphogenesis, neurodevelopment and neurological disorders, and synaptic and neural communication (Fig. 5, D and F; fig. S13, C and D; and tables S4 and S8). In both *NOVA1*$^{hu/hu}$ and *NOVA1*$^{ar/ar}$, lead exposure modified genes crucial for neurodevelopmental disorders. This suggests a potent gene-environment interaction that influences neurodevelopmental outcomes. Next, we used single-cell RNA-seq (scRNA-seq) to untangle cell-specific responses to lead organoid exposure.

scRNA-seq reveals cellular response specificity to lead exposure

We analyzed the scRNA-seq data from COs derived from *NOVA1*$^{hu/hu}$ and *NOVA1*$^{ar/ar}$ treatment conditions. Across all conditions (CTL, 10 μM, and 30 μM), we recovered 99,623 cells (Fig. 6, A and B, and table S9). Eight distinct cell clusters were identified, including Cajal Retzius cells, cortical hem cells, newborn corticofugal projection neurons (CFuPNs), newborn deep-layer projection neurons (DL PNs), projection neurons (PNs), subcortical neurons, apical radial glia (aRG), and an unknown/undefined population (Fig. 6, C and D) (*34*). The *NOVA1*$^{hu/hu}$ CTL organoids contained 39.64% aRG, while the *NOVA1*$^{ar/ar}$ CTL organoids exhibited 48.81% of this cell cluster. In the newborn CFuPN cluster, the *NOVA1*$^{hu/hu}$ CTL organoids comprised 29.68%, compared to 25% in *NOVA1*$^{ar/ar}$ CTL organoids. The cortical hem cluster accounted for 11.56% of the *NOVA1*$^{hu/hu}$ CTL organoids and 10.20% of *NOVA1*$^{ar/ar}$ CTL organoids. For the newborn DL PN cluster, the *NOVA1*$^{hu/hu}$ CTL organoids contained 6.21%, while *NOVA1*$^{ar/ar}$ CTL organoids contained 4.48%. Last, the subcortical neuron cluster comprised 2.80% of the *NOVA1*$^{hu/hu}$ CTL organoids and 1.16% of *NOVA1*$^{ar/ar}$ CTL organoids.

In the lead-treated *NOVA1*$^{hu/hu}$ groups, a reduction in the cortical hem population was observed, decreasing from 11.56% in the CTL to 8.5% in the *NOVA1*$^{hu/hu}$ 10 μM group and 9.29% in the *NOVA1*$^{hu/hu}$ 30 μM group. Conversely, in the newborn CFuPN cluster, an increase was noted, rising from 29.68% in the CTL to 31.79% in the *NOVA1*$^{hu/hu}$ 10 μM group and 33.17% in the *NOVA1*$^{hu/hu}$ 30 μM group (fig. S14, A to E).

Differential gene expression analysis revealed numerous genes uniquely altered in *NOVA1*$^{hu/hu}$ and *NOVA1*$^{ar/ar}$ organoids, with distinct responses to lead exposure in specific cell types. Under untreated conditions, comparisons between *NOVA1*$^{hu/hu}$ and *NOVA1*$^{ar/ar}$ organoids highlighted differentially expressed genes (DEGs) associated with pathways, including regulation of synapse, neuron projection, and brain development (Fig. 6, E and F, and tables S10 to S12). Upon 10 and 30 μM lead exposure, *NOVA1*$^{hu/hu}$ COs exhibited altered gene expression in multiple cell types, with pathways enriched for synapse organization, neuron differentiation, and chemical synapse transmission (fig. S15, A to D, and tables S12 to S14). Similarly, *NOVA1*$^{ar/ar}$ 10 and 30 μM organoids demonstrated lead-induced transcriptional changes with pathways related to neurogenesis, brain development, and synapse function (Fig. 6, G to J, and tables S12, S15, and S16).

One particularly noteworthy gene was *FOXP2*, whose expression varied meaningfully under lead exposure. In *NOVA1*$^{ar/ar}$ organoids, *FOXP2* expression was initially reduced under 10 μM lead but increased following 30 μM lead exposure (Fig. 6K). This biphasic response highlights *FOXP2* as a potential molecular target for understanding the interplay between *NOVA1* archaic variants, lead exposure, and neural development. Building on these transcriptional findings, we next investigated the proteomic landscape of these COs using single-cell proteomics.

Single-cell proteomic insights into neural disruption induced by lead exposure

We performed single-cell proteomics on COs (Fig. 7A) to further elucidate the molecular mechanisms underlying these transcriptional changes. After peptide filtering, we compared *NOVA1*$^{hu/hu}$ and *NOVA1*$^{ar/ar}$ organoids and identified 840 peptides corresponding to 427 proteins (Fig. 7B). Functional analysis revealed that key pathways, such as Rho guanosine triphosphatase (GTPase) signaling—critical for synapse organization and signaling (*35*)—were notably affected (fig. S16).

When comparing *NOVA1*$^{ar/ar}$ untreated and *NOVA1*$^{ar/ar}$ exposed to 10 μM lead, 710 peptides representing 366 proteins were identified after filtering (Fig. 7, C and E). Functional analysis revealed that key pathways, such as the Rho GTPase signaling and nervous system development, are affected (fig. S17, A and B). Biological functions analysis revealed disruptions in pathways linked to nervous system development, axon guidance, and roundabout (ROBO) receptor signaling (fig. S17C). Notably, ROBO receptors, which regulate axonal guidance and growth cone navigation (*36*), were affected. L1CAM, another key protein in neuronal function, was implicated in axon outgrowth and neuronal migration, acting through interactions with the actin cytoskeleton and membrane-cytoskeletal linkers (*37*). These disruptions align with the known roles of ROBO1 in thalamocortical axon extension, which is regulated by activity-dependent transcriptional control, potentially involving the nuclear factor κB complex (*38*).

At 30 μM lead exposure, *NOVA1*$^{ar/ar}$ organoids yielded 684 peptides corresponding to 352 proteins (Fig. 7D). Functional analysis continued highlighting Rho GTPase signaling as meaningfully altered alongside pathways involving the complement system and histone deacetylases (fig. S18A). These findings provide evidence of

Downloaded from https://www.science.org on October 19, 2025

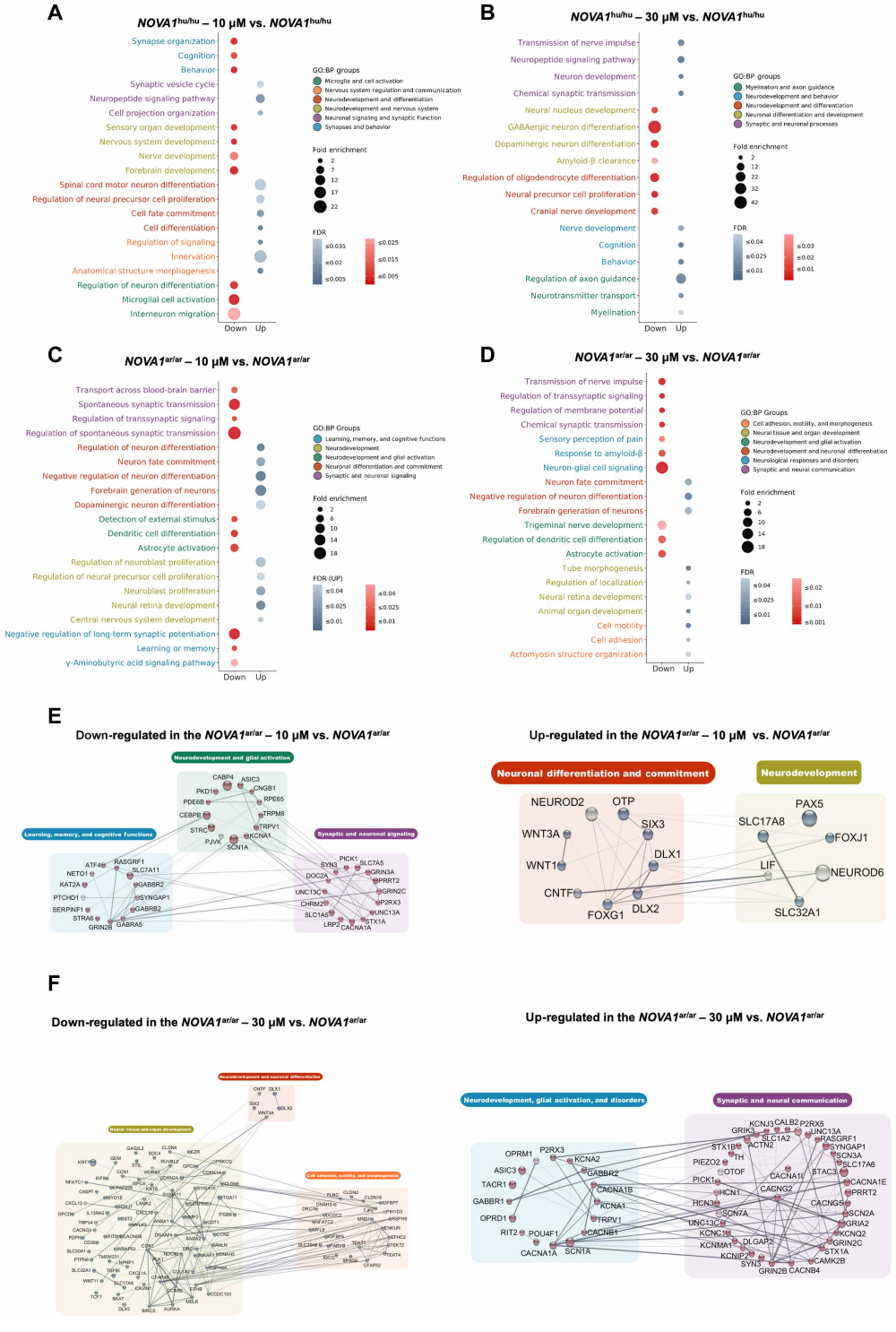

Fig. 5. GO enrichment and gene network analysis of lead-induced changes in *NOVA1* variants. Bubble plots showing the top 20 enriched GO:BP terms (FDR < 0.05; bigger bubbles mean more enrichment) for both the up-regulated (blue) and down-regulated (red) genes in (**A**) *NOVA1*$^{hu/hu}$ treated with 10 μM lead. (**B**) *NOVA1*$^{hu/hu}$ treated with 30 μM lead. (**C**) *NOVA1*$^{ar/ar}$ treated with 10 μM lead. (**D**) *NOVA1*$^{ar/ar}$ treated with 30 μM lead. In all figures, the terms are further organized into major color-coded functional groups; PPIs showing the DEGs representing the major color-coded functional groups are shown in the respective bubble plots. Higher STRINGdb scores (minimum cutoff: 0.4, "medium default confidence") mean less transparency and thicker edges. Higher |L2FC| values mean more prominent nodes, while lower FDR values mean darker (blue, up-regulated; red, down-regulated) nodes in (**E**) *NOVA1*$^{ar/ar}$ treated with 10 μM lead and (**F**) *NOVA1*$^{ar/ar}$ treated with 30 μM lead. Figures S12 and S13 are related to this figure.

Downloaded from https://www.science.org on October 19, 2025

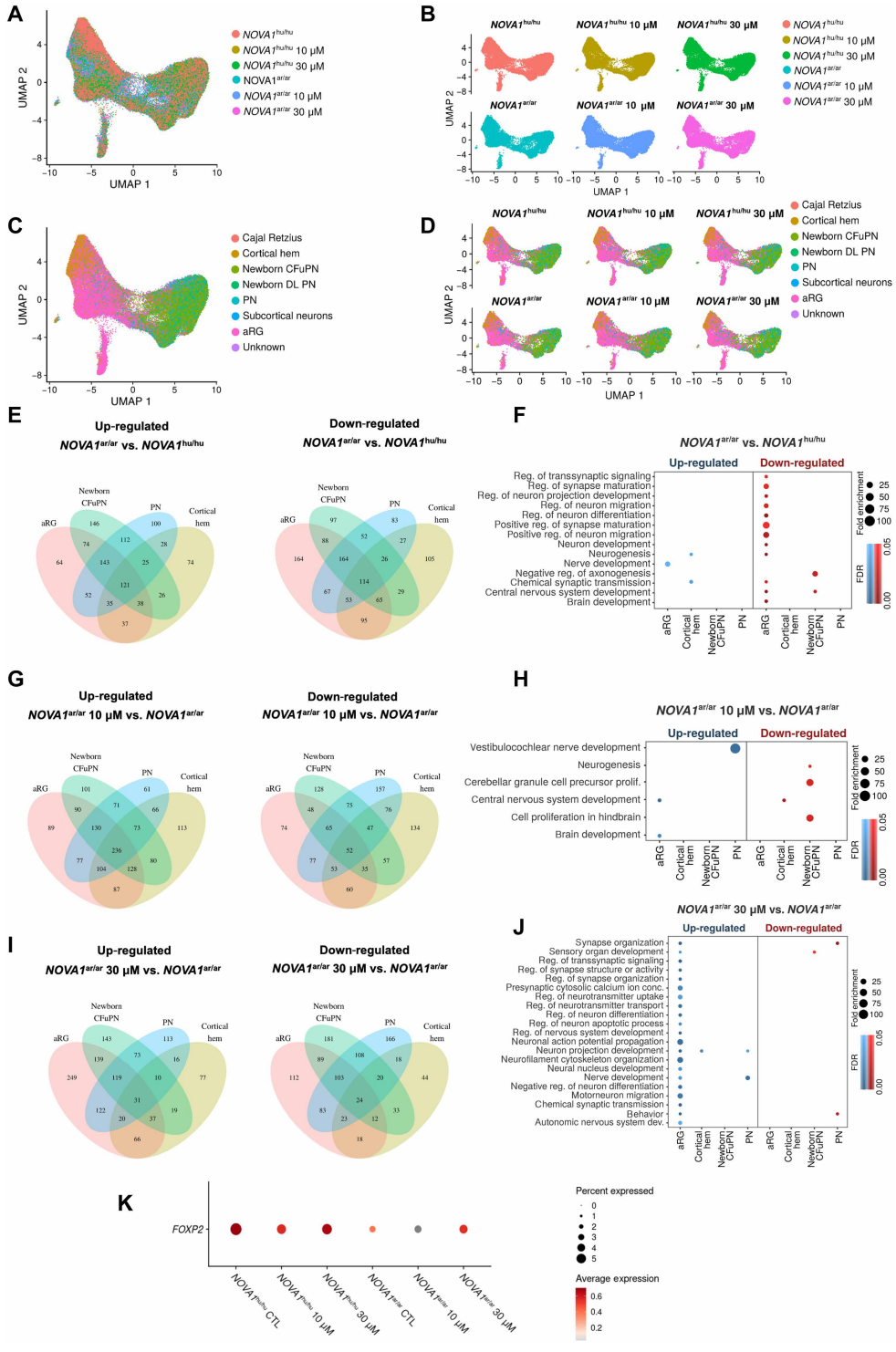

Fig. 6. Lead exposure changes the single-cell transcriptome in *NOVA1*$^{ar/ar}$ COs. (**A** and **B**) Uniform Manifold Approximation and Projection (UMAP) of 99,623 cells from integrated datasets of 60-day-old COs. The integrated dataset is colored by six cellular groups (*NOVA1*$^{hu/hu}$ CTL, $n = 16{,}315$ cells; *NOVA1*$^{hu/hu}$ 10 μM, $n = 16{,}890$ cells; *NOVA1*$^{hu/hu}$ 30 μM, $n = 16{,}268$; *NOVA1*$^{ar/ar}$ CTL, $n = 15{,}411$ cells; *NOVA1*$^{ar/ar}$ 10 μM, $n = 17{,}937$ cells; *NOVA1*$^{ar/ar}$ 30 μM, $n = 16{,}802$ cells). (**C** and **D**) UMAP of *NOVA1*$^{hu/hu}$ and *NOVA1*$^{ar/ar}$ COs treated with different lead concentrations showing eight different clusters. (**E**) Overlap of protein-coding genes up- and down-regulated in *NOVA1*$^{ar/ar}$ versus *NOVA1*$^{hu/hu}$. (**F**) Bubble plot presenting pathways altered in *NOVA1*$^{ar/ar}$. (**G**) Overlap of protein-coding genes up- and down-regulated in *NOVA1*$^{ar/ar}$ 10 μM group versus *NOVA1*$^{ar/ar}$. (**H**) Bubble plot presenting pathways altered in *NOVA1*$^{ar/ar}$ 10 μM group. (**I**) Overlap of protein-coding genes up- and down-regulated in *NOVA1*$^{ar/ar}$ 30 μM group versus *NOVA1*$^{ar/ar}$. (**J**) Bubble plot presenting pathways altered in *NOVA1*$^{ar/ar}$ 30 μM group. (**K**) Bubble plot presenting *FOXP2* expression under all conditions. Figure S14 is related to this figure.

Downloaded from https://www.science.org on October 19, 2025

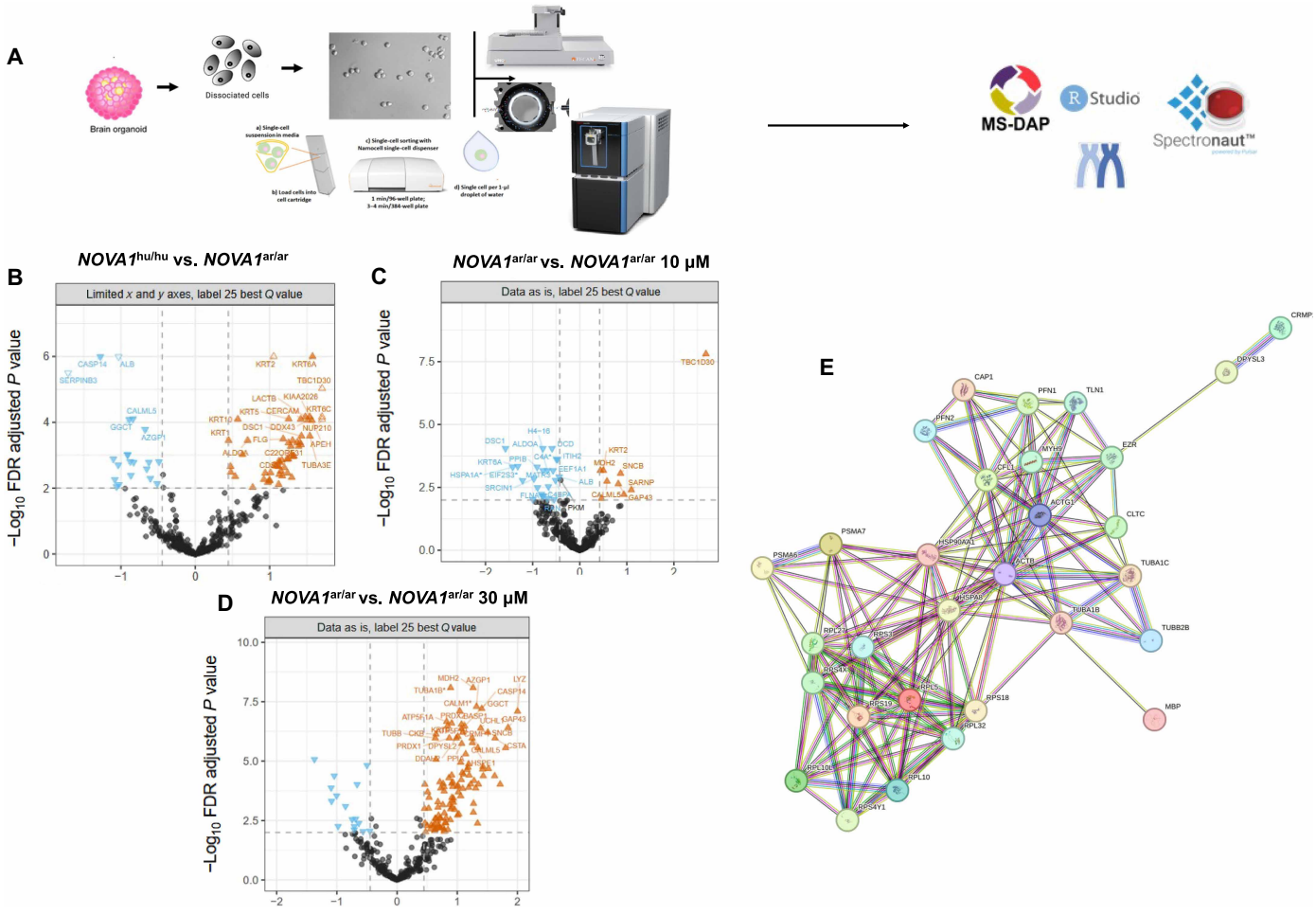

Fig. 7. Lead affects neural pathways in COs at the single-cell proteomics level. (**A**) Schematic representation of the single-cell proteomics protocol. (**B**) Volcano plot of *NOVA1*$^{hu/hu}$ versus *NOVA1*$^{ar/ar}$. A total of 840 peptides were recovered in 427 proteins after peptide filtering (*Q* threshold = 0.01, |L2FC| threshold = 0.445). (**C**) Volcano plot of *NOVA1*$^{ar/ar}$ versus *NOVA1*$^{ar/ar}$ 10 μM group. A total of 710 peptides were recovered in 366 proteins after peptide filter (*Q* threshold = 0.01, |L2FC| threshold = 0.424). (**D**) Volcano plot of *NOVA1*$^{ar/ar}$ versus *NOVA1*$^{ar/ar}$ 30 μM group. A total of 684 peptides were recovered in 352 proteins after peptide filter (*Q* threshold = 0.01, |L2FC| threshold = 0.447). (**E**) Network showing the most important proteins on the pathway. CFL1, Cofilin-1 (required for neural tube morphogenesis and neural crest cell migration); CRMP1, dihydropyrimidinase-related protein 1 (plays a role in axon guidance and, during the axon guidance process, acts downstream of SEMA3A to promote FLNA dissociation from F-actin, which results in the rearrangement of the actin cytoskeleton and the collapse of the growth cone); DPYSL3, dihydropyrimidinase-related protein 3 (plays a role in axon guidance, neuronal growth cone collapse, and cell migration); TUBB2B, tubulin-β 2B chain (plays a critical role in proper axon guidance in central and peripheral axon tracts and is implicated in neuronal migration); MBP, myelin basic protein (plays an important role in the early developing brain long before myelination). Figures S16 to S18 are related to this figure. [(B) to (D)] Full blue arrowheads, down-regulated; empty blue arrowheads, down-regulated and outside plot limits; full orange arrowheads, up-regulated; empty orange arrowheads, up-regulated and outside plots limit; full black dots, not significant; empty black dots, not significant and outside plot limits.

lead's impact on neural development, thalamocortical connections, and its connection to neurodevelopmental disorders.

Integrating single-cell proteomics with transcriptomic data underscores a dynamic interplay between transcriptional and post-transcriptional regulation in cortical brain organoids. Disruptions in pathways such as Rho GTPase signaling, axon guidance, and ROBO receptor activity reveal convergent mechanisms affected by *NOVA1* variants and lead exposure. The identified role of *FOXP2* in transcriptional data correlates with proteomic insights into axonal guidance and thalamocortical connectivity, pointing to its relevance in language development and neurodevelopmental delay (*39*, *40*).

Thalamic organoids show *FOXP2* dysregulation from lead exposure

Considering the observed decrease in *FOXP2* expression in *NOVA1*$^{ar/ar}$ COs (Fig. 6K), the further reduction of this gene's expression following exposure to 10 μM lead, and alterations in the ROBO family identified through single-cell proteomics, we extended our analysis to thalamic organoids (TOs). ROBO1 and *FOXP2* have been previously associated with language and speech disorders (*41*), and *FOXP2* plays a critical role in axonal outgrowth in TOs (*42*). Thus, we investigated *FOXP2* expression in *NOVA1*$^{ar/ar}$ TOs compared to *NOVA1*$^{hu/hu}$ organoids and examined the impact of lead exposure on *NOVA1*$^{ar/ar}$ TOs.

Downloaded from https://www.science.org on October 19, 2025

Thus, we generated TOs following the protocol of Xiang *et al.* (*43*) (Figs. 8 and 9, A and B). Then, we analyzed the scRNA-seq of all *NOVA1*$^{hu/hu}$ and *NOVA1*$^{ar/ar}$ treatment conditions. We recovered 32,125 cells from the *NOVA1*$^{hu/hu}$ (CTL and 10 μM) organoids and 20,957 cells from the *NOVA1*$^{ar/ar}$ (CTL and 10 μM) (Fig. 8, C and D, and table S17) and performed 16,000 reads per cell with more than 2000 genes per cell.

We identified nine cell clusters (Fig. 8, E and F; fig. S19, A to C; and table S13): glutamatergic excitatory neuron (EN1), newborn excitatory neuron (EN2), GABAergic inhibitory neuron 1 (IN1), GABAergic inhibitory neuron 2 (IN2), GABAergic inhibitory neuron 3 (IN3), intermediate progenitor cell 2 (IPC2), neural crest–derived mesenchymal stem cells (MES), radial glia 1 (RG1), and RG2 (*44*). These organoids were positive for TCF7L2, a panthalamic marker, and PAX6, a progenitor marker (Fig. 8, G and H) (*43*), and other markers were analyzed in the scRNA-seq data (Fig. 8I and fig. S19D).

The TCF7L2^{+} TOs also marked for *FOXP2*$^{+}$ and MAP2^{+} cells (Fig. 9A). *FOXP2* is overexpressed in the *NOVA1*$^{ar/ar}$ TO, and when exposed to 10 μM lead, the *FOXP2* expression increased (Fig. 9, B to E). This effect contrasts with the one presented in the COs (Fig. 9B). The expression of *FOXP2* is concentrated in the EN1, EN2, IN1, IN2, and IN3 cell clusters, the same clusters in which *LHX1*, a thalamic marker, is expressed (fig. S19D).

Given *NOVA1*'s established role in brain-specific alternative splicing (*6*, *7*, *45*, *46*), we dissected its splicing regulatory network within scRNA-seq datasets in TO. Upon treatment with lead, we observed altered splicing patterns in *NOVA1*$^{hu/hu}$ organoids. Differential splicing was particularly notable in two genes, *TCF7L2* and *NSD3* (Fig. 9F). In *NOVA1*$^{ar/ar}$ organoids, splicing alterations were observed in four genes after lead exposure: *EDNRB*, *ANKS1A*, *RMDN1*, and *FAM162A* (Fig. 9G). We integrated these genes into a network analysis to further our understanding of these splicing changes. We found that the genes with altered splicing interacted and demonstrated connectivity with key neurological genes, including *NOVA1*, *FOXP2*, *POU3F2*, and *GRID2*. Coexpression and genetic interaction patterns among these genes were substantiated (Fig. 9H). Together, these results indicate that *NOVA1* may be a pivotal node in a complex regulatory network influenced by lead exposure. This complex, including *FOXP2*, a gene essential for language and speech development (*47*, *48*), provides new avenues for understanding cognitive function's genetic and environmental underpinnings and evolution.

DISCUSSION

The presence of lead in teeth from regions of three different continents, covering a period of over 2 million years, supports that exposure to this neurotoxic metal was more prevalent than previously thought (*3*). By analyzing many geographically and ecologically diverse taxa, we observed that lead exposure was not isolated or confined to post-anthropogenic lead release. Still, intermittent exposure to lead from external sources and internal skeletal stores was more likely to be pervasive throughout primate evolution and even more so in hominids.

An unexplored avenue of research is how lead exposure may have affected the health and development of different species throughout hominid evolution. The physiological effects of lead are not limited to disruption of molecular pathways or tissue and organ fidelity but manifest at the population level. Children in communities with a high prevalence of lead toxicity are observed to have lower rates of school completion and higher incidences of criminal and antisocial behavior (*49*). While these outcomes suggest a potential association between lead exposure and decreased social cohesion, they are likely influenced by environmental and socioeconomic factors. Furthermore, the magnitude of these detrimental effects appears to vary across different communities, with a recent study indicating that the negative impact of lead exposure is far more substantial in children experiencing additional socioeconomic disadvantages (*50*).

We observed that *NOVA1*$^{ar/ar}$ organoids exposed to lead exhibited loss of *FOXP2*-expressing neurons and the emergence of a distinct resistant cell population absent in *NOVA1*$^{hu/hu}$ organoids. These data indicate that the archaic variant fails to buffer against lead-induced neuronal stress, supporting the conclusion that it conferred reduced resilience and thus a potential survival disadvantage, under environmental lead exposure. In contrast, the modern human variant offered relative protection against this neurotoxicant. While we acknowledge that primate species have various social behaviors, this finding bolsters our proposition that lead exposure played a noteworthy role in their evolution by affecting neurosocial pathways, such as group-level social cohesion, providing a relative survival advantage to modern humans over Neanderthals.

One major finding of our study involves the lead-induced alteration in *FOXP2* expression within *NOVA1*$^{ar/ar}$ organoids, suggesting a potential interaction between *NOVA1* and *FOXP2* in response to lead exposure. This indicates that *FOXP2* may mediate the neurodevelopmental effects of environmental toxicants, although further research is necessary to confirm this relationship (*39*). The link to childhood apraxia of speech, a rare disorder connected to *FOXP2* mutations, underscores the importance of our observations (*51*). In addition, increased expression of *FOXP2* is associated with the 22q11 neuropsychiatric disorder (*42*), validating the importance of properly regulating its gene expression. Further, the unique *FOXP2* expression in *NOVA1*$^{ar/ar}$ neuronal populations suggests an evolutionary facet to our findings (*52*). This variant may represent a genetic lineage with reduced adaptability to modulate language-related genes such as *FOXP2* (*48*, *53*). We hypothesize that this genetic alteration may have been under negative selection pressure, potentially due to deficits in social or other survival-related advantages. However, further validation is needed to support this proposition (*54*). In addition, we recognize that functional assays, such as electrophysiological measurements and neuronal connectivity studies, would provide additional insights into the impact of *FOXP2* alterations on neuronal development and function. These approaches represent promising avenues for future research to elucidate the mechanistic roles of *FOXP2* in neurodevelopment.

The origins and refinement of language have been vital for human social cohesion and survival. Genes such as *FOXP2* would likely have undergone strong positive selection to aid these processes (*54*). The existence of archaic genetic variants such as *NOVA1*$^{ar/ar}$ offers a compelling avenue for investigating the coevolution of these genes with human neurodevelopment (*10*). While this manuscript was under review, it was recently shown that introducing the human-specific I197V variant of *NOVA1* into mice alters their ultrasonic vocalizations, supporting a functional interaction between *NOVA1* and vocal-related pathways, such as *FOXP2* and other vocalization-related genes that presented binding peaks to *NOVA1* in different brain regions (*55*).

Although our study provides valuable insights, it is important to acknowledge the limitations inherent in using brain organoids as a model system. Brain organoids are a reductionist model system that

Downloaded from https://www.science.org on October 19, 2025

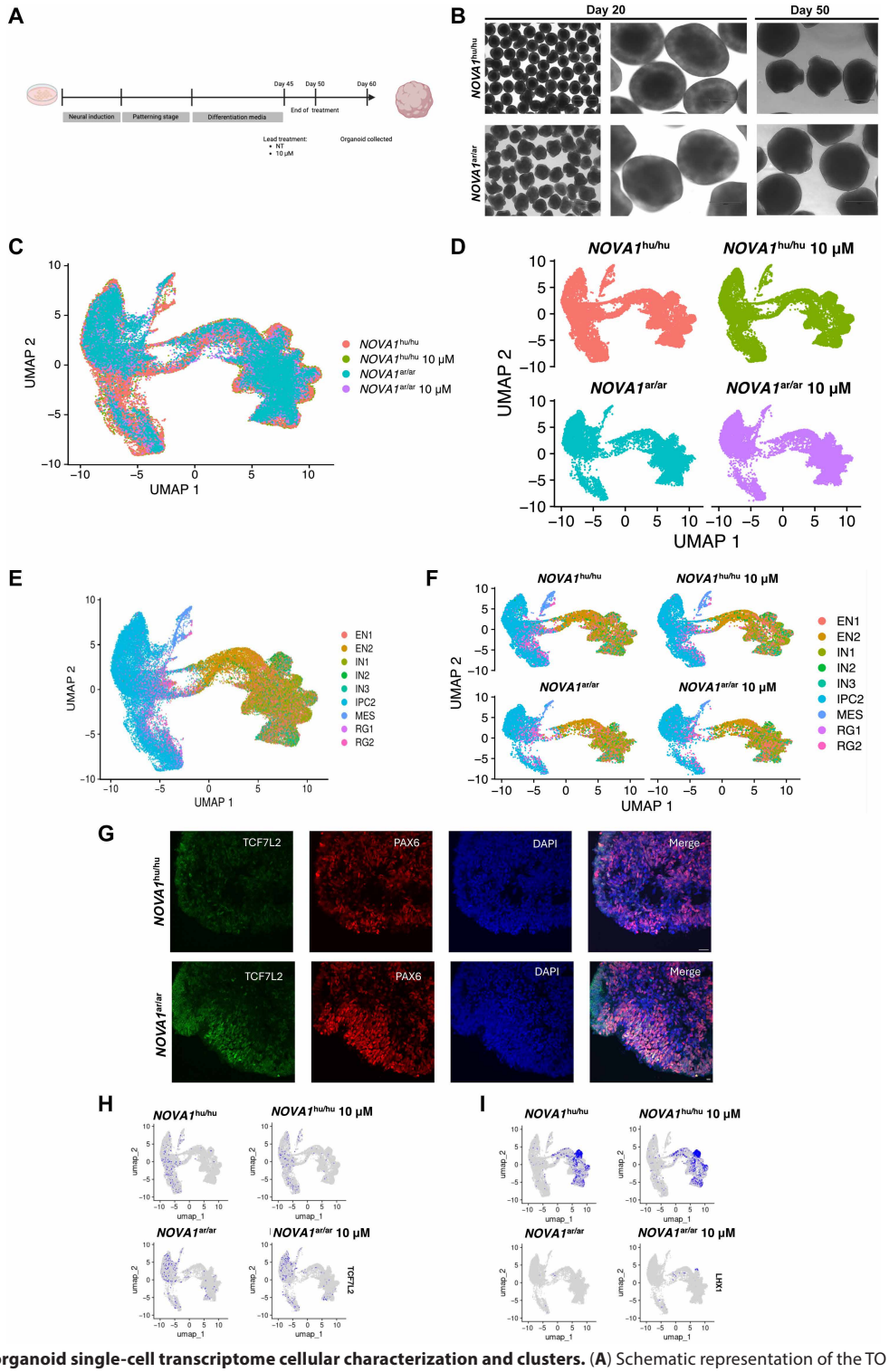

Fig. 8. Thalamic brain organoid single-cell transcriptome cellular characterization and clusters. (**A**) Schematic representation of the TO differentiation protocol. (**B**) Bright-field image of TO at 20 and 50 days. (**C** and **D**) UMAP of 71,942 cells from integrated datasets of 60-day-old TO. The integrated dataset is colored by four cellular groups (*NOVA1*$^{hu/hu}$ CTL, $n = 18{,}932$ cells; *NOVA1*$^{hu/hu}$ 10 µM, $n = 16{,}657$ cells; *NOVA1*$^{ar/ar}$ CTL, $n = 18{,}507$ cells; *NOVA1*$^{ar/ar}$ 10 µM, $n = 17{,}846$ cells). (**E** and **F**) UMAP of *NOVA1*$^{hu/hu}$ and *NOVA1*$^{ar/ar}$ TOs was treated with different lead concentrations, showing nine different clusters. (**G**) Immunohistochemistry image of 60-day-old *NOVA1*$^{hu/hu}$ and *NOVA1*$^{ar/ar}$ TOs. They are TCF7L2^{+} and PAX6^{+} organoids. Scale bar, 50 µm. (**H** and **I**) The expression of *TCF7L2* and *LHX1* are thalamic markers visualized on the UMAP. Figure S19 is related to this figure.

Downloaded from https://www.science.org on October 19, 2025

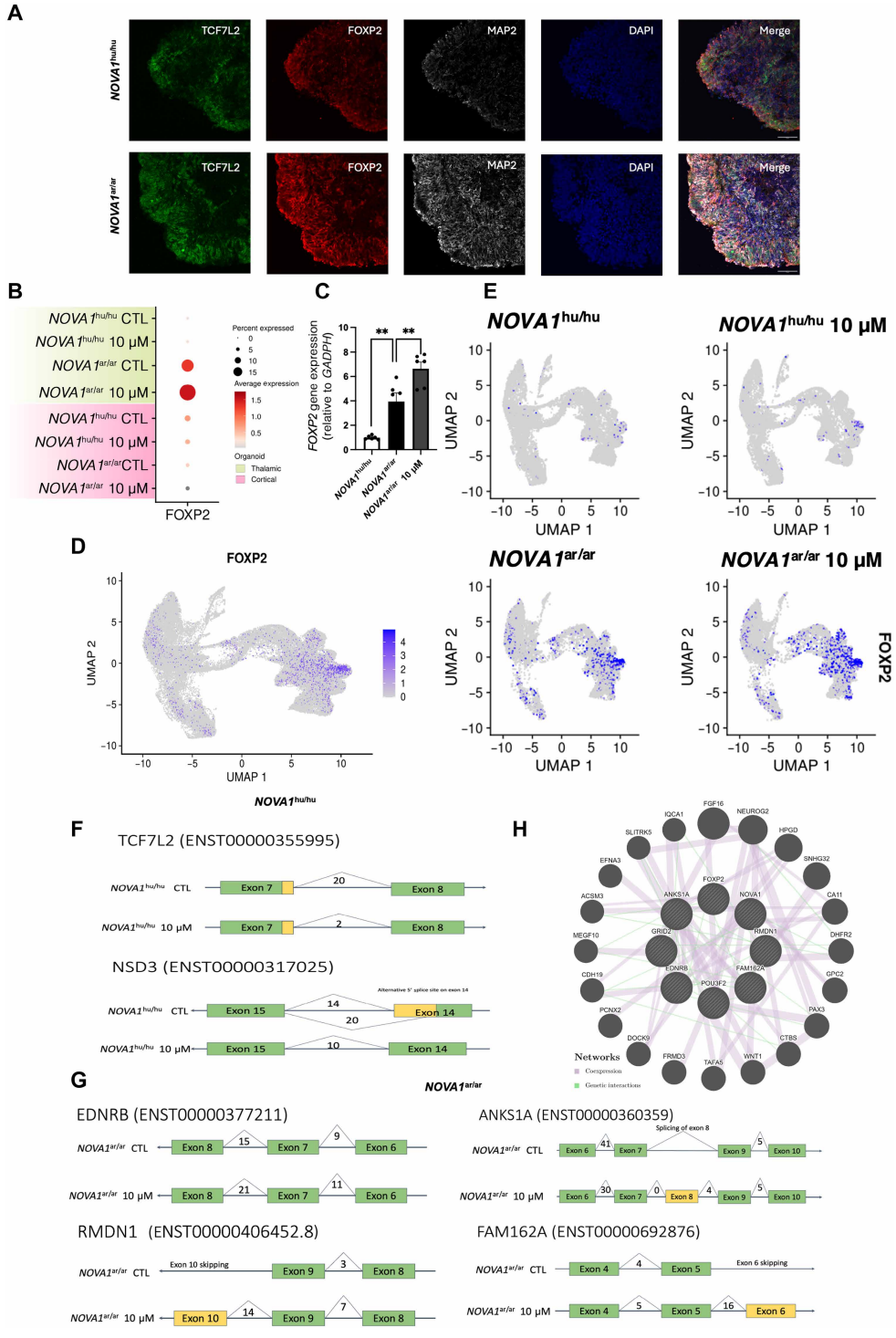

Fig. 9. Exposure to lead increased *FOXP2* gene expression and altered the alternative splicing in *NOVA1*$^{ar/ar}$ in TOs. (**A**) Immunohistochemistry image of 60-day-old *NOVA1*$^{hu/hu}$ and *NOVA1*$^{ar/ar}$ TOs. TOs are TCF7L2^{+}, FOXP2$^{+,}$ and MAP2^{+}. Scale bars, 50 μm. (**B**) Bubble plot showing the gene expression of *FOXP2* in COs and TO. (**C**) Relative expression [reverse transcription quantitative polymerase chain reaction (PCR)] of *FOXP2* in TO of *NOVA1*$^{hu/hu}$, *NOVA1*$^{ar/ar}$, and *NOVA1*$^{ar/ar}$ 10 μM group. $n = 6$ replicates. $^{**}P < 0.01$. (**D** and **E**) UMAP of *NOVA1*$^{hu/hu}$, *NOVA1*$^{hu/hu}$ 10 μM, *NOVA1*$^{ar/ar}$, and *NOVA1*$^{ar/ar}$ 10 μM group showing the cellular expression of *FOXP2*. (**F**) *NOVA1*$^{hu/hu}$ genes that altered their splicing after lead exposure. (**G**) Predicted expression of alternative splicing isoforms based on splice junctions after exposure to 10 and 30 μM in the *NOVA1*$^{ar/ar}$ TO. Reference Sequence accession codes represent gene isoforms, and it is shown, for each condition, a sashimi plot (curvy lines indicate splice junction reads and the number above the spliced reads), indicating the predicted expressed transcript isoform (expression values are indicated by reads per kilobase per million mapped reads). Exons without supporting splice junction reads were not considered expressed and were depleted from the figure to improve visualization. Alternative spliced exons are highlighted in yellow. (**H**) Interaction network of genes that had an alteration in their splicing and *NOVA1*, *FOXP2*, *POU3F2*, and *GRID2*.

Downloaded from https://www.science.org on October 19, 2025

do not fully recapitulate the complexity and functionality of a fully developed human brain (*56*). Although brain organoids offer a unique platform to explore neurodevelopmental processes, they inherently lack several critical aspects of in vivo brain complexity, including vascularization, full cellular diversity, mature neural circuit formation, and interactions with peripheral systems (*57*). Furthermore, organoids primarily reflect early developmental stages and cannot fully model the complexities of later brain maturation. These limitations constrain their ability to recapitulate the intricate evolutionary and functional dynamics of the human brain. Consequently, while our findings provide valuable insights into potential gene-environment interactions, they should be interpreted as initial evidence rather than definitive causal mechanisms. Further research integrating complementary models and in vivo vocalization studies in animal models carrying the human *NOVA1* variant will be essential to bridge the gap between in vitro systems and the complexities of whole organisms.

MATERIALS AND METHODS

Mapping of fossil teeth

Fossil teeth were sectioned with a high-precision diamond saw and polished to 10-μm smoothness. Laser ablation combined with inductively coupled plasma mass spectrometry (LA-ICP-MS) was used for trace elemental mapping analyses of the samples according to the published protocol previously used for Neanderthal samples (*58*). Both Geoarchaeology and Archaeometry Research group (GARG) at Southern Cross University (ESI NW213 coupled to an Agilent 7700 ICP-MS) and Icahn School of Medicine at Mount Sinai in New York (ESI NW193 coupled to an Agilent 8800 ICP-MS) systems were used to map the samples by rastered laser beam along the sample surface in a straight line. The laser spot size was 40 or 35 μm, the laser scan speed was 80 or 70 μm/s, the laser intensity was 80 or 60%, and the ICP-MS total integration time was 0.50 s, producing data points that corresponded to a pixel size of ~40 μm by 40 μm or 35 μm by 35 μm, respectively. NIST610, NIST612, and NIST614 (certified standard reference materials) were used to assess signal drift. Elemental maps were constructed using the interactive R Shiny application "shinyImaging" (http://labs.icahn.mssm.edu/lautenberglab/ to download the application) (*59*). The app transforms individual laser line csv files for each isotope into matrices in counts per second (number of ablation lines multiplied by the number of ablation spots per ablation line). For each element, the gas blank collected during the first 10 s of each laser line was subtracted from the rasterstack, and elements were normalized to ^{43}Ca. Background around the teeth (signal arising from the encasing resin or air) was converted to white coloration (no intensity) to increase clarity of the figures by isolating the dental tissue from its surroundings. Color scales were applied using the linear blue-red lookup table.

Origins of tooth samples

Asia (China and Indonesia)

G. blacki, Pongo sp., and H. sapiens. Fossil teeth from five separate countries were used in this study, seven sites in China (figs. S1 and S2): Queque, Shuangtan, and Chuifeng that all contain *Gigantopithecus* and *Pongo* sp.; Mohui that also contains *H. sapiens* in the upper stratigraphy; and Yicun, Kung Shan, and Shanzu that only contain *Pongo* specimens were analyzed. One site in Indonesia (Lida Ajer) was also analyzed for two *Pongo* teeth. The Chinese sites located in the southern part of the country in the Guangxi province are the oldest in our study for the Asian region (*60*), with Chuifeng and Mohui dated at ~1.9 Ma (*61*, *62*), while Queque is estimated to be mid-Pleistocene using biochronology (*63*) and more recently absolute dating (*11*). All four Chinese sites are karstic caves formed in the limestone formation of the Guangxi province. The two *Pongo* specimens from Indonesia are part of younger assemblages estimated to be late Pleistocene on the basis of the associated fossils. Lida Ajer, a cave site in western Sumatra, Indonesia, contains remnant breccia deposits with a wealth of fossils from rainforest fauna that are associated with two human teeth. The cave was originally excavated in the late 1880s and was only rediscovered a hundred years later by an international team of geochronologists and paleontologists (*64*). A barrage of dating techniques was applied to the sediment around the fossils, to overlying and underlying rock deposits in the cave, and to associated mammal teeth, indicating that the deposit and fossils (including the human teeth) were laid down between 73 and 63 ka ago (*65*).

Africa (South Africa)

A. africanus, P. robustus, and early Homo. The UNESCO World Heritage Site "Fossil Hominids sites of South Africa," colloquially known as the Cradle of Humankind, is situated ~50 km north-northwest of Johannesburg in the Blaauwbank River valley, South Africa (figs. S3 and S4) (*66*). Of particular importance to paleoanthropology, the Sterkfontein and Swartkrans fossil-bearing caves are considered the richest assemblage of australopith fossils in South Africa. Both sites are located in the southern portion of the designated Cradle region. Important fossils of early human evolution have been unearthed at both sites (*67*) and estimated to be early Pleistocene (~2.3 to 1.8 Ma) (*68*).

P. angusticeps. Fossil specimens of *P. angusticeps* were recovered from in situ deposits from the Haasgat paleocave system within the northwestern portion of the UNESCO World Heritage Fossil Hominids Site of South Africa (fig. S5) (*69*). Haasgat is a dolomitic cave system formed within the exposed Malmani Dolomites that was heavily mined in the early 20th century. The in situ fossil beds have been dated to between 2.3 and 1.95 Ma, and most of fossils from the site (including ex situ materials) are interpreted as accumulating near the start of the depositional period at ~2.3 Ma (*70*). In contrast to all the other fossils presented in this study, one Haasgat *P. angusticeps* specimen preserved three mandibular molars (M1, M2, and M3) that were sampled and are presented in this paper.

The modern *Papio ursinus* sample is derived from a single, wild male individual that resided in the mixed grassland and bushveld environs north of Cape Town in the Western Cape Province, South Africa (*71*). This modern sample contrasts with the fossil *P. angusticeps* specimens from the ~2.0-Ma Haasgat fossil locality in several key respects. This includes both geography and topography, as Haasgat ~55 km north of Johannesburg and formed within the rugged hills south of the Magaliesberg mountain range. In addition, combined geomorphological, taphonomic, faunal, and stable isotope data suggest persistent freshwater sources and dense vegetation at Haasgat and consumption of C3 enriched foods by *P. angusticeps* at the site (*69*, *72*).

Europe (France)

Homo neaderthalensis. Payre is an archaeological rock shelter located in a side gorge of the Rhône valley in Southern France with many occupation episodes over the Early Middle Paleolithic (fig. S6). The bedrock at Payre is an Oxfordian well-bedded limestone, which is part of a sedimentary package exposed in the middle Rhône valley (*73*). The assemblage has been extensively studied with identification of lead bands in several Neanderthal teeth (*58*). The dating places the individual in the Mousterian period (late marine isotope stage 7, ~250 ka).

Downloaded from https://www.science.org on October 19, 2025

Oceania (Australia)

P. abelii. The captive orangutan Hsing-Hsing was born in captivity in 1975 at Singapore Zoo and was parent-raised (although additional human feeding cannot be definitively excluded) before being relocated to Perth Zoo in 1983 (fig. S8). His diet would have been radically different to orangutans living in the wild, with limited seasonal influence and no periods of food scarcity. It is expected that the animal and his parents would have had abundant and guaranteed access to food. Lead paint in the enclosure and modern contamination of food cannot be excluded for the provenance of Pb banding in the dental tissues.

Paleoenvironments and diet of studied primates

The primates in this study were living in very different regions, occupying different ecological niches and had thus adapted to various diets. Baboons (modern and fossil) live in various environment and are almost exclusively vegetarian but can adopt opportunistic feeding habits (*74*). Orangutans also follow a vegetarian diet mostly composed of fruits, flower, and leaves and inhabit dense tropical forests (*75*). It has been suggested that *Gigantopithecus* would have inhabited woodland regions with feeding habits closer to modern mountain gorillas, which include fruits, leaves, stems, and possibly tubers (*63*). Apart from *P. robustus*, which is believed to be almost exclusively vegetarian (e.g., sage, nuts and grass) (*76*), all the other hominin specimens (i.e., *Australopithecus* and *Homo*) had adopted an opportunistic omnivore diet with various ecological niches, from hot tropical or grassland-dominated ecosystem in Asia and Africa to the cold taiga biome of Europe. Despite the varied climate and diet experienced across these specimens, discrete regions of elevated lead concentrations were apparent in 73% of samples.

Biodynamics of lead in the environment

Lead is a widespread, naturally occurring element found throughout Earth's crust, practically in all rocks, soils, sediments, and waterways at various concentrations (*77*). The element periodically occurs at unusually high concentrations over large region due to natural geological processes and frequently in association with other metal accumulation. Only a few isotopes of lead are considered stable on the human evolution timescale, including the ^{208}Pb isotopes measured in dental tissues in this study. This stable isotope of lead (^{208}Pb) is produced by the radioactive decay of isotopes of thorium (^{232}Th). Geographic regions can have considerably different lead exposure because of variations in the ages and chemical composition of the rocks and minerals in the local setting. Environmental processes, such as volcanic emissions, wildfires, erosion, and denudation processes, can lead to further accumulation in small areas or dispersal into the environment, particularly waterways and catchments (*77*, *78*). Depending on the concentration, lead can accumulate in minerals (e.g., feldspars, amphiboles, micas, and sulfates) in substitution of other elements, such as potassium, or, if the concentration is sufficiently high, can form lead-rich aggregates or salts (*79*), which will influence its dispersion into the environment. Lead has no physiological function in primates, and high-level exposure has been linked to acute toxicity (*80*). In recent years, with intensification of lead pollution in the environment due to human activity, the element has been extensively investigated, particularly for environmental monitoring and medical-related effects. Animals, including humans, can be exposed to substantial levels of lead by drinking contaminated water, ingesting contaminated food, or inhaling polluted air (e.g., smoke from fire and dust storms) (*81*, *82*). Once lead enters the animal body, the element is stored in bones and teeth, thus reflecting the geographical substrate and ecological setting of the individual. While the bone can store lead for decades (*83*), lead distribution in enamel is stable and does not suffer remobilization. Therefore, the unique developmental pattern of enamel and dentine in incrementing layers offers a temporal record of individual exposure during tissue formation that remains unchanged in adulthood.

Diagenetic process and signal interferences

The typical biogenic signal is readily differentiated from the diagenetic signal. Diagenetic elements are often far more mobile and follow a typical and well-known diffusion pathway that has a broad signature that is unmistakably different from the dental growth patterns that biogenic signals follow (*84*) (fig. S7). Secondary incorporations (diagenesis) of trace elements are typically deposited as diffusion fronts from the roots to the enamel-dentine junction (often with enrichment at the junction) and on the outer layer of the enamel where it is in contact with the sediment (*84*). Because diffusion processes are strongly linked to water circulation, fractures are preferential pathways for elemental mobility. Characteristic patterns of leaching or broad elemental diffusion can be seen associated with these fractures (*84*). ^{238}U and rare earth elements are representative of this specific secondary diffusion through enamel and dentine cracks (fig. S7). The biogenic nature of the signals observed in this study is reinforced by the absence of ^{232}Th in the sample for which ^{208}Pb, a stable isotope of the thorium decay chain, could have been a deposited daughter product (fig. S9). In addition, phosphorus is often measured to quantify potential dissolution episodes of dentine sections through the attack of acidic water. Naturally occurring in hydroxyapatite crystals in teeth, P is mostly absent in reprecipitated crystals of calcite. Large zones in the dentine showing noteworthy depletion of P are considered to be the results of dissolution and recrystallization of dentine, but none match the typical biogenic banding signal (*85*). Although the oldest teeth (e.g., *Australopithecus*, *Gigantopithecus*, and *Pongo*) show some characteristic diagenetic processes, the biogenic Pb signal remains clear (Figs. 2 and 3 and fig. S1).

Lead concentration in permanent teeth

Lead poisoning has been linked to severe debilitating impairments, including gastrointestinal, neuromuscular, and neurological conditions (*86*). Teeth have been shown to offer a more accurate proxy to levels of contamination than bones and sometimes blood, particularly for chronic exposure (*87*–*89*). Epidemiological studies have linked lead exposure to cognitive impairments using the concentration in teeth as a proxy (*90*, *91*). Results show that children with chronic lead exposure (average concentration superior to a few parts per million in dental tissues) had statistically significant cognitive deficiency, social disability, and persistent health issues (*90*–*93*). Even at low concentration, continuous lead exposure was linked to autism syndromes in children (*94*). Fossils presented in this study have an average lead concentration ranging from a few hundred parts per billion to tens of parts per million (see table S1). Teeth from the *Pongo* sp. and *G. blacki* specimens from the sites in China had the highest lead concentrations (some over 50 parts per million). The geochemical maps of both species also show frequent acute exposures. In particular, fossils from the Queque cave system had a substantial level of lead that could have triggered some developmental, health, and perhaps social impairments. It has to be noted that both

Downloaded from https://www.science.org on October 19, 2025

Pongo sp. and *G. blacki* would occupy slightly different ecological niches yet largely overlapping in their geographical range and dietary behavior (*11*). In contrast, teeth from *A. africanus*, *P. robustus*, and early *Homo*, all unearthed from cave systems within close proximity to each other, show very different lead levels. While the geological setting would have been close to identical for all three species, their respective dietary behaviors and likely ecological niches would have been distinctive (*76*, *95*, *96*). Teeth of *A. africanus* show much higher lead levels than teeth of *P. robustus* or early *Homo* (table S1). Teeth of *P. robustus* consistently showed few, low level lead lines, while *A. africanus* and *Homo* sp. show more frequent exposures. The different patterns of lead exposure could suggest that *P. robustus* lead bands were the result of acute exposure (e.g., wild forest fire), while for the other two species, known to have a more varied diet, lead bands may be due to more frequent, seasonal, and higher lead concentration through bioaccumulation processes in the food chain (*97*). These results indicate that throughout human evolution lead has been a pervasive source of heavy metal contamination, which seems to have been more or less acute according not only to the geographical settings but also to the dietary behavior of the hominid. Considering the potential effect of bioaccumulation of lead with trophic level, it is interesting to consider the role the element played in the cognitive development of early humans ancestors shifting toward a more carnivorous diet (*98*).

iPSC lines and cell culture

The iPSC lines used here were previously generated and characterized using two different genetic backgrounds, with several clones isolated from each line (*6*). As previously described (*31*, *32*, *99*, *100*), we maintained human iPSC (hiPSC) colonies on Matrigel-coated (BD Biosciences, San Jose, CA, USA) 6-cm plates. We kept the cells in mTeSR plus (STEMCELL Technologies, Vancouver, Canada), changing the medium every other day. We exclusively used cell cultures that tested negative for mycoplasma contamination. The experiments adhered to the ethical principles of the WMA Declaration of Helsinki and the Belmont Report by the US Department of Health and Human Services. The study received approval from the UCSD IRB/ESCRO committee under protocol 141223.

Generation of cortical and thalamic brain organoids

We generated COs following previously described protocols (*6*, *29*–*32*). Briefly, we cultured hiPSCs for ~6 days and then dissociated them with 1:1 Accutase (Life Technologies):phosphate-buffered saline (PBS). Subsequently, we plated the cells into a six-well plate (4×10^6 cells per well) in mTeSR plus supplemented with 10 μM SB43-1542 (SB; Stemgent, Cambridge, MA, USA), 1 μM dorsomorphin (Dorso; R&D Systems, Minneapolis, MN, USA), and 5 μM Y-27632 (EMD Millipore, Burlington, MA, USA). The cells were then cultured in shaker suspension (95 rpm at 37°C). We fed them mTeSR plus supplemented with 10 μM SB and 1 μM Dorso to nourish the emerging spheres for 3 days. Subsequently, the medium was changed to Media1 [Neurobasal (Life Technologies), 1× GlutaMAX (Life Technologies), 2% Gem21 NeuroPlex (Gem21; GeminiBio, Sacramento, CA, USA), 1% N2 NeuroPlex (N2; GeminiBio), 1% nonessential amino acids (NEAAs; Life Technologies), 1% penicillin/streptomycin (P/S; Life Technologies), 10 μM SB, and 1 μM Dorso] and cultivated every other day for 6 days. Afterward, we started the proliferation stage and used Media2 (Neurobasal, 1× GlutaMAX, 2% Gem21, 1% NEAA, and 1% P/S) supplemented with fibroblast growth factor 2 (FGF-2) (20 ng/ml; Life Technologies) daily for 7 days. After the first step of proliferation stage, we followed a second stage of cell proliferation using Media2 supplemented with FGF-2 and epidermal growth factor (20 ng/ml each; PeproTech, Rocky Hill, NJ, USA) every other day for 6 days. For the subsequent 6 days, we cultured the organoids in Media2 supplemented with brain-derived neurotrophic factor (BDNF), glial cell line–derived neurotrophic factor, and neurotrophin-3 (10 ng/ml each; all PeproTech), 200 μM L-ascorbic acid (Sigma-Aldrich, St. Louis, MO, USA), and 1 mM dibutyryl–adenosine 3′,5′-monophosphate (Sigma-Aldrich) every other day. Last, we maintained the COs until day 45 in Media2 without supplementation. At day 45, we treated the organoids with 10 or 30 μM lead(II) acetate trihydrate (Sigma-Aldrich, St. Louis, MO, USA) and changed the medium every 3 days. After 10 days of treatment, we changed the medium for Media2 without lead acetate and collected the organoids for scRNA-seq, bulk RNA-seq, and immunofluorescence after 5 days.

We generated TOs following the previously described protocol (*43*) with some modifications. The iPSCs were dissociated into single cells using Accutase. The single cells were suspended in induction medium composed of Dulbecco's modified Eagle's medium (DMEM)–F12 supplemented with 15% KnockOut Serum Replacement, 1% minimum essential medium (MEM) NEAAs, 1% GlutaMAX, 100 mM β-mercaptoethanol, 100 nM LDN-193189, 10 μM SB-431542, insulin (4 μg/ml), 5% heat-inactivated fetal bovine serum (FBS), and 50 μM Y27632. Around 2.5×10^6 cells were plated in AgreWell 800 plate per well (STEMCELL Technologies) for the spheroid formation until the next day. On day 2, the cells were transferred to a six-well ultralow-attachment plate using the medium with the same composition from the first day, but without FBS, and the organoids were kept in the shaker with 95 rpm. On days 4 and 6, the medium was modified by removing both FBS and Y27632. From days 8 to 16, the organoids were cultured in a patterning medium consisting of DMEM-F12, 0.15% dextrose, 100 mM β-mercaptoethanol, 1% N2 supplement, and 2% B27 supplement without vitamin A, along with bone morphogenetic protein 7 (30 ng/ml) and 1 μM PD325901. The medium was changed every other day. From day 16 onward, differentiation medium was used, containing a 1:1 mixture of DMEM-F12 and Neurobasal medium, supplemented with 0.5% N2 supplement, 1% B27 supplement, 0.5% MEM-NEAA, 1% GlutaMAX, 0.025% insulin, 50 mM β-mercaptoethanol, and 1% P/S, along with BDNF (20 ng/ml) and 200 μM ascorbic acid. Medium changes were performed every other day until day 25 and subsequently every 4 days. At day 45, we treated the organoids with 10 μM lead(II) acetate trihydrate (Sigma-Aldrich, St. Louis, MO, USA) and changed the medium every 3 days. After 10 days of treatment, we changed the medium for differentiation medium with BDNF (20 ng/ml) and 200 μM ascorbic acid without lead acetate. We collected the organoids for scRNA-seq and immunofluorescence after 5 days.

Immunofluorescence staining of brain organoids

We conducted immunofluorescence staining following previously described methods (*6*, *29*–*32*). We fixed the cortical brain organoids for 4 hours in 4% paraformaldehyde, then transferred them to 30% sucrose, and embedded them in O.C.T. (Sakura, Tokyo, Japan). Subsequently, we sectioned the organoids at 20 μm using a cryostat. The resulting organoid sections on slides were air dried, permeabilized, and blocked using 0.1% Triton X-100 and 3% bovine serum albumin in PBS.

Downloaded from https://www.science.org on October 19, 2025

We applied primary antibodies (chicken anti-MAP2, Abcam, ab5392, 1:1000; rabbit anti-FOXG1, Abcam, 196868, 1:500; mouse anti-SOX2, Abcam, ab79351, 1:500; rabbit anti-TCF7L2, Cell Signaling Technology, 2569, 1:100; mouse anti-PAX6, BD Biosciences, BDB561462, 1:500; mouse anti-*FOXP2*, Millipore, MABE415, 1:250) diluted in blocking buffer and incubated them overnight at 4°C. After washing the slides three times with PBS (each for 5 min), we incubated them with secondary antibodies (Alexa Fluor 555, Alexa Fluor 647, and Alexa Fluor 488, Life Technologies) diluted 1:1000 in a blocking buffer. We stained the cell nuclei with 4′,6-diamidino-2-phenylindole (DAPI) (diluted 1:10,000 in PBS) for 5 min. Last, we mounted the slides with ProLong Gold anti-fade mountant (Life Technologies) and captured and analyzed the images using a Z1 Axio Observer Apotome fluorescence microscope (Zeiss, Oberkochen, Germany).

Cell cycle assay

We conducted the cell cycle assay, a previously established method (*6*, *101*, *102*). COs and neural progenitor cells were dissociated and counted using the NucleoCounter NC-3000 with a Via1-Cassette (Chemometec, Allerod, Denmark). The dissociated cells were fixed either on ice or at 4°C using 70% ethanol for a minimum of 2 hours. Subsequently, the cells were resuspended in a solution containing DAPI (0.5 μg/ml) and 0.1% Triton X-100 in PBS and incubated at 37°C for 5 min. The cells were then distributed onto an NC-Slide A2 chamber (Chemometec), and fluorescence was measured using the NucleoCounter NC-3000, following the manufacturer's instructions.

Bulk RNA-seq

We had 24 duplicated samples (48 in total) from two batches (1 and 2), all coming from cortical human brain organoids of four cell lineages: the isogenic pair ASC/C136 (line 1) and another isogenic pair *NOVA1*-C15/*NOVA1*-C27 (line 2). ASC and *NOVA1*-C27 have the "modern" version of the NOVA1 gene (Hu/Hu), while C136 and *NOVA1*-C15 have a modified "archaic" version of the gene (Ar/Ar). All samples were divided into three groups: CTL (not treated) and treated with either 10 or 30 μM lead. After the initial quality check, we decided to proceed only with the 24 duplicated samples from the high-quality data of batch 2.

First, we performed quality checks on the Illumina HiSeq paired-end (2× 150 bp) FASTQ files. The mean quality score per base was 35.53, where 91.61% had an optimal quality superior to 30. We used the tool FastQC (v0.11.9; www.bioinformatics.babraham.ac.uk/projects/fastqc/) to generate the quality metrics. After that, the tool MultiQC (v1.17) (*103*) was used to summarize all the results produced by FastQC for all files (for details, check our GitHub repository—link available in the "Data and materials availability" section). Pseudoalignment without bootstraps was made with Kallisto (v0.46.2) (*104*) and consisted of two steps: (i) creation of the reference "index" (all parameters default) (ii) and then the "quant" command (all parameters default; we adjusted the number of threads and random-access memory to optimize the performance) command to generate the quantification matrix. The metrics available by Kallisto itself indicate high-quality results, as the percentage of reads pseudoaligned was always around 90% (table S18). We used GENCODE (v36) as the reference transcriptome (*105*) and GRCh38 (hg38) as the human reference genome (*106*). All map files were also created at this step of the pipeline.

The abundance files produced by Kallisto were previously used as inputs for the following steps in R (v4.3.1). Initially, their raw counts were transformed ("lengthScaledTPM" method) from transcripts to genes with TXimport (v1.24.0) (*107*). Then, we used the DESeq2 (v1.36.0) (*108*) tool to run the differential expression analysis on all genes using two replicates. We performed several comparisons, and the control group is always indicated when appropriate. The TPM values were rounded, as required by the tool, and genes with counts less than one were removed. The *P* values were further adjusted (FDR) on the basis of the less conservative correction method of Benjamini-Hochberg. In the end, we applied extra final filters on the outputs of DESeq2 to extract only the more biologically meaningful candidates. Therefore, genes with $|L2FC| > 1$ ($\log_2$ fold change) and FDR < 0.05 were included in the downstream analyses.

GO enrichment analyses

We used the biological process (BP) terms curated from the GO Consortium (*109*) for the enrichment analyses. First, we performed the analyses, separating the up- and down-regulated genes for each desired comparison. Then, we uploaded the list of genes to the web tool ShinyGO (v0.81) (*110*), setting the FDR cutoff to 0.05 and the pathway minimum size to 10. Then, to summarize the generally long list of GO Biological Processes (GO:BPs) and remove redundant terms, we used the online tool REVIGO (v1.8.1) (*111*). The resulting list was set to be small (0.5) and without obsolete GO terms. The default SimRel semantic similarity measure was selected.

After that, the shorter list was uploaded in ChatGPT (v4) (from OpenAI; https://openai.com; the exact commands can be found in our public GitHub repository). In summary, we used ChatGPT to help select only terms (top 10 whenever possible to facilitate the interpretation of the results) associated with brain, neurodevelopment and nervous system, organ functions (such as learning and memory), and neurological disorders. In addition, we also used ChatGPT to assist in grouping the GO terms into the major categories (two or three to enhance the results' relevance seen in figures such as bubble plots and protein-protein interactions (PPIs). Last, it is worth mentioning that all artificial intelligence (AI) outputs were always double checked by the team after each step to ensure compatibility (consistent and real GO:BP term names and IDs) between the final list and the raw one initially provided as input.

The PPIs were made in Cytoscape (v3.10.0) (*112*) by uploading the list of DEG—up- and down-regulated genes separately—in the tool and importing the full STRING network (protein query) through the STRINGdb app (v2.2.0) (*113*), which integrates the STRING database (*114*) to Cytoscape. We opted to leave the confidence score cutoff at 0.4 ("medium"; default) and increased it to a "high" confidence whenever possible, as long as the general structure of the network remained similar to the original. Moreover, we did not include additional interactors. The degree sorted circle layout was chosen whenever possible, with minor node label position adjustments to make the gene names visible. The STRINGdb score was used to adjust both the transparency and the thickness of the edges, whereas the L2FC and FDR values—imported from an external metadata table—were used to change the size and the color of the nodes, respectively. Higher scores mean darker and thicker edges, while bigger and darker nodes mean more significant (lower FDR) and meaningful (greater L2FC in up-regulated DEGs and lower in down-regulated DEGs) genes. Figures such as the bubble plots were further edited in Inkscape (v1.2) (https://inkscape.org) when formatting was necessary.

Downloaded from https://www.science.org on October 19, 2025

AmpliDrop scRNA-seq analysis

We analyzed single-cell reads obtained from 60-day-old organoids using the same protocol outlined in the original study by Trujillo and colleagues (*6*, *29*) and Xiang and colleagues (*43*). We performed scRNA-seq in 16 libraries of dissociated cells, 12 libraries of cortical brain organoids, *NOVA1*$^{hu/hu}$ (CTL, 10 μM, and 30 μM), and the *NOVA1*$^{ar/ar}$ (CTL, 10 μM, and 30 μM), and 4 libraries of thalamic brain organoids *NOVA1*$^{hu/hu}$ (CTL and 10 μM) and the *NOVA1*$^{ar/ar}$ (CTL and 10 μM). The organoids were dissociated to a single cell using Accutase (Thermo Fisher Scientific) and papain/deoxyribonuclease (Worthington) and mechanical dissociation using a 1000-μl pipette. After dissociation, the cells were counted, and the viability was analyzed. We dissociated the cells for 50 min, and every 10 min, we mechanically dissociated the cells until we had only single cells in suspension. The protocol of the scRNA-seq was executed by the Universal Sequencing Technology Corporation (Carlsbad, CA). Briefly, they used the innovative AmpliDrop technology. Single-cell suspensions underwent processing for single-cell library generation. Fixed cells were subjected to permeabilization, reverse transcription, and tagmentation, with the treated cells subsequently individually encapsulated within water-in-oil droplets, generated via controlled pipetting in polymerase chain reaction (PCR) tubes. Within these droplets, tagged cDNA within a cell was amplified, along with unique barcode tags, facilitated by a MiniAmp Thermal Cycler (Thermo Fisher Scientific), resulting in amplified 3′ end cDNA fragments, each marked with a cell-specific barcode. Following this, Illumina sequencing adapters were incorporated into the barcoded cDNA to complete the construction of single-cell libraries. Clean-up and size selection procedures were executed using HighPrep PCR Clean-up MagBio magnetic beads (MagBio Genomics), and library quantification and sizing were carried out using the High Sensitivity D1000 Screen Tape and the 4150 TapeStation System (Agilent Technologies). Ultimately, sequencing was performed on the NextSeq instrument (Illumina), generating single-end reads with an average of 10,500 to 17,500 reads per cell. After the scRNA-seq data acquisition, the processed fastq files were analyzed employing the AmpliDrop Downstream Analysis v1.0 developed by Universal Sequencing Technology Corp.

scRNA-seq analysis

Quality control and data filtering, normalization, scaling, dimensionality reduction, expression analysis, and visualization were conducted using the R package Seurat (v5.0.0) (*115*). First, Seurat objects were independently created from each sample, adhering to specific criteria (min.cells = 3 and min.features = 200). Cells deviating from the range of 200 to 3000 features and those harboring over 5% of reads from mitochondrial genes were considered low quality and excluded from further analysis. Doublets were detected and removed using the R package scDblFinder (v1.16.0) (*116*). Data normalization and scaling were executed through the NormalizeData() and ScaleData() Seurat functions, respectively, with a scale factor set at 10,000. Data integration was based on 2000 highly variable genes using the FindVariableFeatures() function (selection.method = vst), and anchors between individual samples were pinpointed using the FindIntegrationAnchors() function (dims = 1:20). These anchors were subsequently used in the IntegrateData() function (dims = 1:20) to construct a batch-corrected expression matrix encompassing all cells. Cellular identities were inferred by projecting reference datasets from previous studies onto the current datasets. This was achieved using the Seurat functions FindIntegrationAnchors (dims = 1:20) and IntegrateData (dims = 1:20), which facilitated the alignment and integration of the reference data, enabling the classification of cells based on their similarity to the reference annotations. For scRNA-seq data from TOs, reference cell populations were derived from developing human thalamic neurons (*44*), while COs were classified using reference cell populations identified in developing human COs at 1.5- and 2-month time points (*34*). Principal components analysis and Uniform Manifold Approximation and Projection (UMAP) dimension reduction were performed using the RunPCA() and RunUMAP() Seurat functions (npcs = 30; dims = 1:20), respectively. To identify DEGs between cell populations of COs, we used the FindMarkers() Seurat function (logfc.threshold = 0.1; min.pct = 0.01). Only genes with absolute average |L2FC| > 0.1 and Bonferroni-adjusted $P < 0.05$ were considered as differentially expressed. GO:BP enrichment analyses were conducted on genes uniquely differentially expressed in each cell population compared to all others using the R package clusterProfiler (v4.14.4; default parameters) (*117*). Only GO terms with FDR-adjusted $P < 0.05$ were considered enriched, and redundant GO terms were further filtered using the REVIGO web tool (*111*). Bubble plots for enriched GO terms were created using the R package ggplot2 (v3.5.1).

Single-cell proteomics analytical method

All of the single-cell proteomics samples were analyzed using a Thermo Fisher Scientific Vanquish Neo ultrahigh-performance liquid chromatography system coupled to a Thermo Fisher Scientific Orbitrap Astral mass spectrometer equipped with an EASY-Spray source. Each of the individual single-cell tryptic digests were injected directly from a 384-well multiwell plate. Fast sample loading was performed with combined pressure and flow rate control where the maximum pressure was set to 700 bar and the flow rate capped at 1 μl/min. Using direct injections, peptides were separated on a 50-cm Thermo Fisher Scientific EASY-Spray high-performance liquid chromatography column with a 75-μm inside diameter and 2-μm bead size at a flow rate of 300 nl/min with the column heated to 60°C. Separations were performed with a 36-min gradient from 3 to 40% B where mobile phase A was 0.1% formic acid in water and mobile phase B was 80% acetonitrile and 0.1% formic acid in water. For MS1 analyses, MS1 spectra were acquired in the Orbitrap every 0.6 s at a resolution of 240,000 with a precursor mass range from 400 to 1000. For MS2 analyses, data were acquired in data-independent acquisition (DIA) mode with a normalized higher-energy collisional dissociation collision energy set to 25% and a default charge state of 2. Nonoverlapping DIA precursor isolation windows were set to 20 mass/charge ratio spanning 400 to 1000 (same as MS1 range) with a maximum injection time of 50 ms and a normalized automatic gain control target value of 800%.

Single-cell alternative splicing analysis

For the single-cell alternative splice analysis, we quantified both annotated and novel splice junctions using STARsolo (STAR v.2.7.6) with the parameter set to --soloFeatures SJ. Splice junctions were filtered to retain those with a minimum count of 10 and deemed differentially expressed under the conditions. We assessed the resulting junctions using Integrative Genomics Viewer (*118*). Sashimi plots were created using rmats2sashimiplot (https://github.com/Xinglab/rmats2sashimiplot), based on annotation files derived from the alignment and the coordinates of the selected events during manual

Downloaded from https://www.science.org on October 19, 2025

inspection of Splice Junction counts. In addition, we explored gene interaction networks through the software GeneMANIA (https://genemania.org/).

Statistical analysis for brain organoid study

We conducted statistical analyses using GraphPad Prism v9 software (GraphPad Software, La Jolla, CA). Sample sizes were determined on the basis of previous publications from our laboratory and other relevant sources. Experiment-specific information regarding samples and cell lines can be found in the figure legends. Samples were allocated and evaluated on the basis of genotype, and randomization was not applied. Outliers in other experiments were identified and excluded on the basis of GraphPad criteria. Continuous variables were presented as means ± SEM, and 95% confidence intervals were calculated on the basis of normal distribution assumptions. Normality was assessed visually or through analysis in GraphPad, and variance was considered in all analyses. For comparisons between groups, means of continuous variables were analyzed using appropriate statistical tests, such as unpaired Student's *t* test, one-way or two-way analysis of variance (ANOVA), or Mann-Whitney *U* test for nonparametric distributions. Two-sided tests were performed, and the significance level (α) was set at 0.05.

Use of AI for GO term curation

We used the AI tool ChatGPT-4 (GPT-4-turbo), developed by OpenAI, version dated December 2024, to assist in the curation and structuring of GO:BP terms. The AI was used to filter, modify, and organize GO terms provided by the authors according to specific criteria relevant to neurobiology, including brain, neuron and glia function, synapses, the blood-brain barrier, neurodevelopment, cognition, memory, motor skills, and neurological disorders. Eight structured prompt sessions were conducted, each corresponding to differential gene expression profiles (up-regulated/down-regulated) across conditions ($NOVA1^{Hu/Hu}$ and $NOVA1^{Ar/Ar}$ at 10 and 30 μM). Prompts included instructions to (i) filter provided GO terms to retain only those directly relevant to nervous system function; (ii) modify specific GO term names and IDs while ensuring the final selections remained consistent with the original list format; (iii) reformat lists into various requested structures, including line-separated IDs and tab-delimited tables; (iv) categorize final GO terms into two to three nonoverlapping functional groups with a minimum of three terms per group, under thematic labels such as "synaptic and neural communication," "neurodevelopment," or "cognition and behavior."

The final outputs, including updated GO IDs, names, and group classifications, were integrated into our analyses and used for downstream interpretation of pathway enrichment and biological significance. The full prompt is provided in table S19, and the final curated and categorized list of GO:BP terms, including modified IDs, names, and functional group assignments generated with the assistance of ChatGPT-4 (GPT-4-turbo), is provided in table S20.

Supplementary Materials

The PDF file includes:
Figs. S1 to S19
Tables S1 and S2, S19 and S20
Legends for tables S3 to S18

Other Supplementary Material for this manuscript includes the following:
Tables S3 to S18

REFERENCES AND NOTES

1. B. C. Trumble, C. E. Finch, The exposome in human evolution: From dust to diesel. *Q. Rev. Biol.* **94**, 333–394 (2019).
2. S. Hong, J.-P. Candelone, C. C. Patterson, C. F. Boutron, Greenland ice evidence of hemispheric lead pollution two millennia ago by greek and roman civilizations. *Science* **265**, 1841–1843 (1994).
3. D. R. Smith, A. R. Flegal, Lead in the biosphere: Recent trends. *Ambio* **24**, 21–23 (1995).
4. P. J. Bushnell, R. E. Bowman, Effects of chronic lead ingestion on social development in infant rhesus monkeys. *Neurobehav. Toxicol.* **1**, 207–219 (1979).
5. H. L. Needleman, C. A. Gatsonis, Low-level lead exposure and the IQ of children: A meta-analysis of modern studies. *JAMA* **263**, 673–678 (1990).
6. C. A. Trujillo, E. S. Rice, N. K. Schaefer, I. A. Chaim, E. C. Wheeler, A. A. Madrigal, J. Buchanan, S. Preissl, A. Wang, P. D. Negraes, R. A. Szeto, R. H. Herai, A. Huseynov, M. S. A. Ferraz, F. S. Borges, A. H. Kihara, A. Byrne, M. Marin, C. Vollmers, A. N. Brooks, J. D. Lautz, K. Semendeferi, B. Shapiro, G. W. Yeo, S. E. P. Smith, R. E. Green, A. R. Muotri, Reintroduction of the archaic variant of *NOVA1* in cortical organoids alters neurodevelopment. *Science* **371**, eaax2537 (2021).
7. J. Ule, A. Ule, J. Spencer, A. Williams, J. S. Hu, M. Cline, H. Wang, T. Clark, C. Fraser, M. Ruggiu, B. R. Zeeberg, D. Kane, J. N. Weinstein, J. Blume, R. B. Darnell, Nova regulates brain-specific splicing to shape the synapse. *Nat. Genet.* **37**, 844–852 (2005).
8. Y. Xin, Z. Li, H. Zheng, J. Ho, M. T. V. Chan, W. K. K. Wu, Neuro-oncological ventral antigen 1 (*NOVA1*): Implications in neurological diseases and cancers. *Cell Prolif.* **50**, e12348 (2017).
9. N. N. Parikshak, V. Swarup, T. G. Belgard, M. Irimia, G. Ramaswami, M. J. Gandal, C. Hartl, V. Leppa, L. T. Ubieta, J. Huang, J. K. Lowe, B. J. Blencowe, S. Horvath, D. H. Geschwind, Genome-wide changes in lncRNA, splicing, and regional gene expression patterns in autism. *Nature* **540**, 423–427 (2016).
10. A. R. Muotri, "Archealization" of human brain organoids. *Neuropsychopharmacology* **47**, 401–402 (2022).
11. Y. Zhang, K. E. Westaway, S. Haberle, J. K. Lubeek, M. Bailey, R. Ciochon, M. W. Morley, P. Roberts, J.-x. Zhao, M. Duval, A. Dosseto, Y. Pan, S. Rule, W. Liao, G. A. Gully, M. Lucas, J. Mo, L. Yang, Y. Cai, W. Wang, R. Joannes-Boyau, The demise of the giant ape *Gigantopithecus blacki*. *Nature* **625**, 535–539 (2024).
12. P. Budd, J. Montgomery, J. Evans, B. Barreiro, Human tooth enamel as a record of the comparative lead exposure of prehistoric and modern people. *Sci. Total Environ.* **263**, 1–10 (2000).
13. G. Monge, F. J. Jimenez-Espejo, A. García-Alix, F. Martínez-Ruiz, N. Mattielli, C. Finlayson, N. Ohkouchi, M. C. Sánchez, J. M. B. de Castro, R. Blasco, J. Rosell, J. Carrión, J. Rodríguez-Vidal, G. Finlayson, Earliest evidence of pollution by heavy metals in archaeological sites. *Sci. Rep.* **5**, 14252 (2015).
14. M. J. Kohn, M. J. Schoeninger, W. W. Barker, Altered states: Effects of diagenesis on fossil tooth chemistry. *Geochim. Cosmochim. Acta* **63**, 2737–2747 (1999).
15. E. A. Hinz, M. J. Kohn, The effect of tissue structure and soil chemistry on trace element uptake in fossils. *Geochim. Cosmochim. Acta* **74**, 3213–3231 (2010).
16. B. Gulson, A. Taylor, J. Eisman, Bone remodeling during pregnancy and post-partum assessed by metal lead levels and isotopic concentrations. *Bone* **89**, 40–51 (2016).
17. C. Austin, T. M. Smith, R. M. Farahani, K. Hinde, E. A. Carter, J. Lee, P. A. Lay, B. J. Kennedy, B. Sarrafpour, R. J. Wright, R. O. Wright, M. Arora, Uncovering system-specific stress signatures in primate teeth with multimodal imaging. *Sci. Rep.* **6**, 18802 (2016).
18. M. F. Skinner, Developmental stress in South African hominins: Comparison of recurrent enamel hypoplasias in *Australopithecus africanus* and *Homo naledi*. *S. Af. J. Sci.* **115**, 1–10 (2019).
19. P. D. Gluckman, M. A. Hanson, F. M. Low, Evolutionary and developmental mismatches are consequences of adaptive developmental plasticity in humans and have implications for later disease risk. *Philos. Trans. R. Soc. Lond. B Biol. Sci.* **374**, 20180109 (2019).
20. S. J. Nelson, M. M. Ash, *Wheeler's Dental Anatomy, Physiology, and Occlusion* (Saunders, ed. 9, 2010).
21. M. A. S. Laidlaw, H. W. Mielke, G. M. Filippelli, D. L. Johnson, C. R. Gonzales, Seasonality and children's blood lead levels: Developing a predictive model using climatic variables and blood lead data from Indianapolis, Indiana, Syracuse, New York, and New Orleans, Louisiana (USA). *Environ Health Perspect* **113**, 793–800 (2005).
22. K. Rajakumar, M. F. Holick, C. G. Moore, E. Cohen, F. Olabopo, M. A. Haralam, J. Bogusz, A. Nucci, S. L. Greenspan, Impact of seasonal flux on 25-hydroxyvitamin D and bone turnover in pre- and early pubertal youth. *Pediatr. Int.* **56**, 35–42 (2014).
23. W. I. Manton, C. R. Angle, K. L. Stanek, D. Kuntzelman, Y. R. Reese, T. J. Kuehnemann, Release of lead from bone in pregnancy and lactation. *Environ. Res.* **92**, 139–151 (2003).
24. R. Gwiazda, C. Campbell, D. Smith, A noninvasive isotopic approach to estimate the bone lead contribution to blood in children: Implications for assessing the efficacy of lead abatement. *Environ. Health Perspect.* **113**, 104–110 (2005).
25. M. Rauchenzauner, A. Schmid, P. Heinz-Erian, K. Kapelari, G. Falkensammer, A. Griesmacher, G. Finkenstedt, W. Högler, Sex- and age-specific reference curves for

Downloaded from https://www.science.org on October 19, 2025

serum markers of bone turnover in healthy children from 2 months to 18 years. *J. Clin. Endocrinol. Metabol.* **92**, 443–449 (2007).
26. R. W. Hornung, B. P. Lanphear, K. N. Dietrich, Age of greatest susceptibility to childhood lead exposure: A new statistical approach. *Environ. Health Perspect.* **117**, 1309–1312 (2009).
27. P. Jiang, Z. Hou, J. M. Bolin, J. A. Thomson, R. Stewart, RNA-Seq of human neural progenitor cells exposed to lead (Pb) reveals transcriptome dynamics, splicing alterations and disease risk associations. *Toxicol. Sci.* **159**, 251–265 (2017).
28. R. H. Herai, R. A. Szeto, C. A. Trujillo, A. R. Muotri, Response to comment on "Reintroduction of the archaic variant of *NOVA1* in cortical organoids alters neurodevelopment". *Science* **374**, eabi9881 (2021).
29. C. A. Trujillo, R. Gao, P. D. Negraes, J. Gu, J. Buchanan, S. Preissl, A. Wang, W. Wu, G. G. Haddad, I. A. Chaim, A. Domissy, M. Vandenberghe, A. Devor, G. W. Yeo, B. Voytek, A. R. Muotri, Complex oscillatory waves emerging from cortical organoids model early human brain network development. *Cell Stem Cell* **25**, 558–569.e7 (2019).
30. C. A. Trujillo, J. W. Adams, P. D. Negraes, C. Carromeu, L. Tejwani, A. Acab, B. Tsuda, C. A. Thomas, N. Sodhi, K. M. Fichter, S. Romero, F. Zanella, T. J. Sejnowski, H. Ulrich, A. R. Muotri, Pharmacological reversal of synaptic and network pathology in human MECP2-KO neurons and cortical organoids. *EMBO Mol. Med.* **13**, e12523 (2021).
31. P. Mesci, J. S. de Souza, L. Martin-Sancho, A. Macia, A. Saleh, X. Yin, C. Snethlage, J. W. Adams, S. H. Avansini, R. H. Herai, A. Almenar-Queralt, Y. Pu, R. A. Szeto, G. Goldberg, P. T. Bruck, F. Papes, S. K. Chanda, A. R. Muotri, SARS-CoV-2 infects human brain organoids causing cell death and loss of synapses that can be rescued by treatment with sofosbuvir. *PLOS Biol.* **20**, e3001845 (2022).
32. F. Papes, A. P. Camargo, J. S. de Souza, V. M. A. Carvalho, R. A. Szeto, E. LaMontagne, J. R. Teixeira, S. H. Avansini, S. M. Sánchez-Sánchez, T. S. Nakahara, C. N. Santo, W. Wu, H. Yao, B. M. P. Araújo, P. E. N. F. Velho, G. G. Haddad, A. R. Muotri, Transcription factor 4 loss-of-function is associated with deficits in progenitor proliferation and cortical neuron content. *Nat. Commun.* **13**, 2387 (2022).
33. M. Q. Fitzgerald, T. Chu, F. Puppo, R. Blanch, M. Chillon, S. Subramaniam, A. R. Muotri, Publisher correction: Generation of 'semi-guided' cortical organoids with complex neural oscillations. *Nat. Protoc.*, s41596-024-01087-8 (2024).
34. A. Uzquiano, A. J. Kedaigle, M. Pigoni, B. Paulsen, X. Adiconis, K. Kim, T. Faits, S. Nagaraja, N. Antón-Bolaños, C. Gerhardinger, A. Tucewicz, E. Murray, X. Jin, J. Buenrostro, F. Chen, S. Velasco, A. Regev, J. Z. Levin, P. Arlotta, Proper acquisition of cell class identity in organoids allows definition of fate specification programs of the human cerebral cortex. *Cell* **185**, 3770–3788.e27 (2022).
35. J. G. Duman, S. Mulherkar, Y. K. Tu, J. X. Cheng, K. F. Tolias, Mechanisms for spatiotemporal regulation of Rho-GTPase signaling at synapses. *Neurosci. Lett.* **601**, 4–10 (2015).
36. M. O'Donnell, R. K. Chance, G. J. Bashaw, Axon growth and guidance: Receptor regulation and signal transduction. *Annu. Rev. Neurosci.* **32**, 383–412 (2009).
37. G. H. Poplawski, A. K. Tranziska, I. Leshchyns'ka, I. D. Meier, T. Streichert, V. Sytnyk, M. Schachner, L1CAM increases MAP2 expression via the MAPK pathway to promote neurite outgrowth. *Mol. Cell Neurosci.* **50**, 169–178 (2012).
38. E. Mire, C. Mezzera, E. Leyva-Díaz, A. V. Paternain, P. Squarzoni, L. Bluy, M. Castillo-Paterna, M. J. López, S. Peregrín, M. Tessier-Lavigne, S. Garel, J. Galcerán, J. Lerma, G. López-Bendito, Spontaneous activity regulates Robo1 transcription to mediate a switch in thalamocortical axon growth. *Nat. Neurosci.* **15**, 1134–1143 (2012).
39. G. Konopka, J. M. Bomar, K. Winden, G. Coppola, Z. O. Jonsson, F. Gao, S. Peng, T. M. Preuss, J. A. Wohlschlegel, D. H. Geschwind, Human-specific transcriptional regulation of CNS development genes by FOXP2. *Nature* **462**, 213–217 (2009).
40. O. Nagy, J. Kárteszi, B. Elmont, A. Ujfalusi, Case report: Expressive speech disorder in a family as a hallmark of 7q31 deletion involving the FOXP2 Gene. *Front. Pediatr.* **9**, 664548 (2021).
41. C. Boeckx, A. Benítez-Burraco, Globularity and language-readiness: Generating new predictions by expanding the set of genes of interest. *Front. Psychol.* **5**, 1324 (2014).
42. D. Shin, C. N. Kim, J. Ross, K. M. Hennick, S. R. Wu, N. Paranjape, R. Leonard, J. C. Wang, M. G. Keefe, B. J. Pavlovic, K. C. Donohue, C. Moreau, E. M. Wigdor, H. H. Larson, D. E. Allen, C. R. Cadwell, A. Bhaduri, G. Popova, C. E. Bearden, A. A. Pollen, S. Jacquemont, S. J. Sanders, D. Haussler, A. P. Wiita, N. A. Frost, V. S. Sohal, T. J. Nowakowski, Thalamocortical organoids enable in vitro modeling of 22q11.2 microdeletion associated with neuropsychiatric disorders. *Cell Stem Cell* **31**, 421–432.e8 (2024).
43. Y. Xiang, Y. Tanaka, B. Cakir, B. Patterson, K. Y. Kim, P. Sun, Y. J. Kang, M. Zhong, X. Liu, P. Patra, S. H. Lee, S. M. Weissman, I. H. Park, hESC-derived thalamic organoids form reciprocal projections when fused with cortical organoids. *Cell Stem Cell* **24**, 487–497.e7 (2019).
44. C. N. Kim, D. Shin, A. Wang, T. J. Nowakowski, Spatiotemporal molecular dynamics of the developing human thalamus. *Science* **382**, eadf9941 (2023).
45. K. B. Jensen, B. K. Dredge, G. Stefani, R. Zhong, R. J. Buckanovich, H. J. Okano, Y. Y. Yang, R. B. Darnell, Nova-1 regulates neuron-specific alternative splicing and is essential for neuronal viability. *Neuron* **25**, 359–371 (2000).
46. R. J. Buckanovich, R. B. Darnell, The neuronal RNA binding protein Nova-1 recognizes specific RNA targets in vitro and in vivo. *Mol. Cell Biol.* **17**, 3194–3201 (1997).
47. P. Hunter, The riddle of speech: After FOXP2 dominated research on the origins of speech, other candidate genes have recently emerged. *EMBO Rep.* **20**, e47618 (2019).
48. J. den Hoed, K. Devaraju, S. E. Fisher, Molecular networks of the FOXP2 transcription factor in the brain. *EMBO Rep.* **22**, e52803 (2021).
49. R. Nevin, How lead exposure relates to temporal changes in IQ, violent crime, and unwed pregnancy. *Environ Res.* **83**, 1–22 (2000).
50. A. T. Marshall, S. Betts, E. C. Kan, R. McConnell, B. P. Lanphear, E. R. Sowell, Association of lead-exposure risk and family income with childhood brain outcomes. *Nat. Med.* **26**, 91–97 (2020).
51. C. M. Vicario, FOXP2 gene and language development: The molecular substrate of the gestural-origin theory of speech? *Front. Behav. Neurosci.* **7**, 99 (2013).
52. S. Ma, M. Skarica, Q. Li, C. Xu, R. D. Risgaard, A. T. N. Tebbenkamp, X. Mato-Blanco, R. Kovner, Ž. Krsnik, X. de Martin, V. Luria, X. Martí-Pérez, D. Liang, A. Karger, D. K. Schmidt, Z. Gomez-Sanchez, C. Qi, K. T. Gobeske, S. Pochareddy, A. Debnath, C. J. Hottman, J. Spurrier, L. Teo, A. G. Boghdadi, J. Homman-Ludiye, J. J. Ely, E. W. Daadi, D. Mi, M. Daadi, O. Marín, P. R. Hof, M.-R. Rasin, J. Bourne, C. C. Sherwood, G. Santpere, M. J. Girgenti, S. M. Strittmatter, A. M. M. Sousa, N. Sestan, Molecular and cellular evolution of the primate dorsolateral prefrontal cortex. *Science* **377**, eabo7257 (2022).
53. P. Deriziotis, S. E. Fisher, Neurogenomics of speech and language disorders: The road ahead. *Genome Biol.* **14**, 204 (2013).
54. P. Lieberman, The evolution of language and thought. *J. Anthropol. Sci.* **94**, 127–146 (2016).
55. Y. Tajima, C. D. M. Vargas, K. Ito, W. Wang, J. D. Luo, J. Xing, N. Kuru, L. C. Machado, A. Siepel, T. S. Carroll, E. D. Jarvis, R. B. Darnell, A humanized NOVA1 splicing factor alters mouse vocal communications. *Nat. Commun.* **16**, 1542 (2025).
56. C. A. Trujillo, A. R. Muotri, Brain organoids and the study of neurodevelopment. *Trends Mol. Med.* **24**, 982–990 (2018).
57. H. Setia, A. R. Muotri, Brain organoids as a model system for human neurodevelopment and disease. *Semin. Cell Dev. Biol.* **95**, 93–97 (2019).
58. T. M. Smith, C. Austin, D. R. Green, R. Joannes-Boyau, S. Bailey, D. Dumitriu, S. Fallon, R. Grün, H. F. James, M.-H. Moncel, I. S. Williams, R. Wood, M. Arora, Wintertime stress, nursing, and lead exposure in Neanderthal children. *Sci. Adv.* **44**, eaau9483 (2018).
59. M. Niedzwiecki, C. Austin, R. Remark, M. Merad, S. Gnjatic, G. Estrada-Gutierrez, A. Espejel-Nunez, H. Borboa-Olivares, M. Guzman-Huerta, R. Wright, R. Wright, M. Arora, A multimodal imaging workflow to visualize metal mixtures in the human placenta and explore colocalization with biological response markers. *Metallomics* **8**, 444–452 (2016).
60. L. X. Zhao, L. Z. Zhang, New fossil evidence and diet analysis of *Gigantopithecus blacki* and its distribution and extinction in South China. *Quat. Int.* **286**, 69–74 (2013).
61. Q. Shao, W. Wang, C. Deng, P. Voinchet, M. Lin, A. Zazzo, E. Douville, J.-M. Dolo, C. Falguères, J.-J. Bahain, ESR, U-series and paleomagnetic dating of *Gigantopithecus fauna* from Chuifeng Cave, Guangxi, southern China. *Quat. Res.* **82**, 270–280 (2014).
62. Q. Shao, J.-J. Bahain, W. Wang, M. Zhu, P. Voinchet, M. Lin, E. Douville, Coupled ESR and U-series dating of early Pleistocene *Gigantopithecus* faunas at Mohui and Sanhe Caves, Guangxi, southern China. *Quat. Geochronol.* **30**, 524–528 (2015).
63. Y. Zhang, T. Harrison, *Gigantopithecus blacki*: A giant ape from the Pleistocene of Asia revisited. *Am. J. Phys. Anthropol.* **162**, 153–177 (2017).
64. M. E. F. T. Dubois, "Voorlopig bericht omtrent het onderzoek naar de Pleistocene en Tertiaire vertebraten-fauna van Sumatra en Java, gedurende het jaar 1890," in *Nat Tijdschr Ned Indië* (Ernst, 1891), vol. 51, pp. 93–100.
65. K. E. Westaway, J. Louys, R. D. Awe, M. J. Morwood, G. J. Price, J. X. Zhao, M. Aubert, R. Joannes-Boyau, T. M. Smith, M. M. Skinner, T. Compton, R. M. Bailey, G. D. van den Bergh, J. de Vos, A. W. G. Pike, C. Stringer, E. W. Saptomo, Y. Rizal, J. Zaim, W. D. Santoso, A. Trihascaryo, L. Kinsley, B. Sulistyanto, An early modern human presence in Sumatra 73,000–63,000 years ago. *Nature* **548**, 322–325 (2017).
66. R. Joannes-Boyau, J. W. Adams, C. Austin, M. Arora, I. Moffat, A. I. R. Herries, M. P. Tonge, S. Benazzi, A. R. Evans, O. Kullmer, S. Wroe, A. Dosseto, L. Fiorenza, Elemental signatures of *Australopithecus africanus* teeth reveal seasonal dietary stress. *Nature* **572**, 112–115 (2019).
67. R. Broom, New fossil anthropoid skull from South Africa. *Nature* **138**, 486–488 (1936).
68. A. I. R. Herries, R. Pickering, J. W. Adams, D. Curnoe, G. Warr, A. G. Latham, J. Shaw, "A multi-disciplinary perspective on the age of *Australopithecus* in Southern Africa," in *The Paleobiology of Australopithecus*, K. E. Reed, J. G. Fleagle, R. E. Leakey, Eds. (Springer Netherlands, 2013), pp. 21–40.
69. J. W. Adams, A revised listing of fossil mammals from the Haasgat cave system ex situ deposits (HGD), South Africa. *Palaeontol. Electronica* **15**, 1–88 (2012).
70. P. Kappen, A. Kegley, D. Patterson, D. Howard, M. de Jonge, S. Potze, J. Adams, Palaeomagnetic and synchrotron analysis of >1.95 Ma fossil-bearing palaeokarst at Haasgat, South Africa. *S. Af. J. Sci.* **110**, 1–12 (2014).

Downloaded from https://www.science.org on October 19, 2025

71. L. Mucina, M. C. Rutherford, *The vegetation of South Africa, Lesotho and Swaziland* (2006), vol. 19.
72. J. Adams, A. Kegley, J. Krigbaum, New faunal stable carbon isotope data from the Haasgat HGD assemblage, South Africa, including the first reported values for *Papio angusticeps* and *Cercopithecoides haasgati*. *J. Hum. Evol.* **64**, 693–698 (2013).
73. C. Bureau de Recherches Géologiques et Minières., Ed. (1976a), vol. 842.
74. B. Shorrocks, *The Biology of African Savannahs* (Oxford Univ. Press, 2007).
75. H. Pontzer, D. Raichlen, R. Shumaker, C. Ocobock, S. Wich, Metabolic adaptation for low energy throughput in orangutans. *Proc. Natl. Acad. Sci. U.S.A.* **107**, 14048–14052 (2010).
76. A. Peterson, E. F. Abella, F. E. Grine, M. F. Teaford, P. S. Ungar, Microwear textures of *Australopithecus africanus* and *Paranthropus robustus* molars in relation to paleoenvironment and diet. *J. Hum. Evol.* **119**, 42–63 (2018).
77. P. B. Tchounwou, C. G. Yedjou, A. K. Patlolla, D. J. Sutton, Heavy metal toxicity and the environment. *Exp. Suppl.* **101**, 133–164 (2012).
78. R. A. Wuana, F. E. Okieimen, Heavy metals in contaminated soils: A review of sources, chemistry, risks and best available strategies for remediation. *ISRN Ecol.* **2011**, 402647 (2011).
79. M. L. Brännvall, H. Kurkkio, R. Bindler, O. Emteryd, I. Renberg, The role of pollution versus natural geological sources for lead enrichment in recent lake sediments and surface forest soils. *Environ. Geol.* **40**, 1057–1065 (2001).
80. S. Tong, Y. E. von Schirnding, T. Prapamontol, Environmental lead exposure: A public health problem of global dimensions. *Bull. World Health Organ.* **78**, 1068–1077 (2000).
81. I. Renberg, M. W. Persson, O. Emteryd, Pre-industrial atmospheric lead contamination detected in Swedish lake sediments. *Nature* **368**, 323–326 (1994).
82. Y. Erel, J. J. Morgan, The relationships between rock-derived lead and iron in natural waters. *Geochim. Cosmochim. Acta* **56**, 4157–4167 (1992).
83. E. J. O'Flaherty, Physiologically based models for bone-seeking elements. IV. Kinetics of lead disposition in humans. *Toxicol. Appl. Pharmacol.* **118**, 16–29 (1993).
84. R. Grün, M. Aubert, R. Joannes-Boyau, M.-H. Moncel, High resolution analysis of uranium and thorium concentration as well as U-series isotope distributions in a Neanderthal tooth from Payre (Ardèche, France) using laser ablation ICP-MS. *Geochim. Cosmochim. Acta* **72**, 5278–5290 (2008).
85. E. A. Abou Neel, A. Aljabo, A. Strange, S. Ibrahim, M. Coathup, A. M. Young, L. Bozec, V. Mudera, Demineralization-remineralization dynamics in teeth and bone. *Int. J. Nanomed.* **11**, 4743–4763 (2016).
86. J. M. Pearce, Burton's line in lead poisoning. *Eur. Neurol.* **57**, 118–119 (2007).
87. M. Arora, B. J. Kennedy, S. Elhlou, N. J. Pearson, D. M. Walker, P. Bayl, S. W. Y. Chan, Spatial distribution of lead in human primary teeth as a biomarker of pre- and neonatal lead exposure. *Sci. Total Environ.* **371**, 55–62 (2006).
88. M. Manea-Krichten, C. Patterson, G. Miller, D. Settle, Y. Erel, Comparative increases of lead and barium with age in human tooth enamel, rib and ulna. *Sci. Total Environ.* **107**, 179–203 (1991).
89. T. Sanders, Y. Liu, V. Buchner, P. B. Tchounwou, Neurotoxic effects and biomarkers of lead exposure: A review. *Rev. Environ. Health* **24**, 15–45 (2009).
90. G. Winneke, U. Krämer, A. Brockhaus, U. Ewers, G. Kujanek, H. Lechner, W. Janke, Neuropsychological studies in children with elevated tooth-lead concentrations - II. Extended Study. *Int. Arch. Occup. Environ. Health* **51**, 231–252 (1983).
91. B. Kamberi, L. Kqiku, V. Hoxha, E. Dragusha, Lead concentrations in teeth from people living in Kosovo and Austria. *Coll. Antropol.* **35**, 79–82 (2011).
92. H. L. Needleman, C. McFarland, R. B. Ness, S. E. Fienberg, M. J. Tobin, Bone lead levels in adjudicated delinquents: A case control study. *Neurotoxicol. Teratol.* **24**, 711–717 (2002).
93. D. K. Marcus, J. J. Fulton, E. J. Clarke, Lead and conduct problems: A meta-analysis. *J. Clin. Child Adolesc. Psychol.* **39**, 234–241 (2010).
94. M. Arora, A. Reichenberg, C. Willfors, C. Austin, C. Gennings, S. Berggren, P. Lichtenstein, H. Anckarsäter, K. Tammimies, S. Bölte, Fetal and postnatal metal dysregulation in autism. *Nat. Commun.* **8**, 15493 (2017).
95. M. Sponheimer, J. A. Lee-Thorp, Isotopic evidence for the diet of an early hominid, *Australopithecus africanus*. *Science* **283**, 368–370 (1999).
96. D. S. Strait, G. W. Weber, S. Neubauer, J. Chalk, B. G. Richmond, P. W. Lucas, M. A. Spencer, C. Schrein, P. C. Dechow, C. F. Ross, I. R. Grosse, B. W. Wright, P. Constantino, B. A. Wood, B. Lawn, W. L. Hylander, Q. Wang, C. Byron, D. E. Slice, A. L. Smith, The feeding biomechanics and dietary ecology of *Australopithecus africanus*. *Proc. Natl. Acad. Sci. U.S.A.* **106**, 2124–2129 (2009).
97. D. Kundu, S. Mondal, D. Dutta, S. Haque, A. Ghosh, Accumulation and contamination of lead in different trophic levels of food chain in sewage-fed East Kolkata Wetland, West Bengal, India. *Int. J. Environ. Technol. Sci.* **2**, 61–68 (2016).
98. V. Balter, J. Braga, P. Telouk, J. F. Thackeray, Evidence for dietary change but not landscape use in South African early hominins. *Nature* **489**, 558–560 (2012).
99. J. S. de Souza, C. Carromeu, L. B. Torres, B. H. Araujo, F. R. Cugola, R. M. Maciel, A. R. Muotri, G. Giannocco, IGF1 neuronal response in the absence of MECP2 is dependent on TRalpha 3. *Hum. Mol. Genet.* **26**, 270–281 (2017).
100. J. S. de Souza, D. R. Ferreira, R. Herai, C. Carromeu, L. B. Torres, B. H. S. Araujo, F. Cugola, R. M. B. Maciel, A. R. Muotri, G. Giannocco, Altered gene expression of thyroid hormone transporters and deiodinases in iPS MeCP2-knockout cells-derived neurons. *Mol. Neurobiol.* **56**, 8277–8295 (2019).
101. K. Griesi-Oliveira, A. Acab, A. R. Gupta, D. Y. Sunaga, T. Chailangkarn, X. Nicol, Y. Nunez, M. F. Walker, J. D. Murdoch, S. J. Sanders, T. V. Fernandez, W. Ji, R. P. Lifton, E. Vadasz, A. Dietrich, D. Pradhan, H. Song, G. L. Ming, X. Gu, G. Haddad, M. C. Marchetto, N. Spitzer, M. R. Passos-Bueno, M. W. State, A. R. Muotri, Modeling non-syndromic autism and the impact of TRPC6 disruption in human neurons. *Mol. Psychiatry* **20**, 1350–1365 (2015).
102. P. D. Negraes, C. A. Trujillo, N. K. Yu, W. Wu, H. Yao, N. Liang, J. D. Lautz, E. Kwok, D. McClatchy, J. Diedrich, S. M. de Bartolome, J. Truong, R. Szeto, T. Tran, R. H. Herai, S. E. P. Smith, G. G. Haddad, J. R. Yates, A. R. Muotri, Altered network and rescue of human neurons derived from individuals with early-onset genetic epilepsy. *Mol. Psychiatry* **26**, 7047–7068 (2021).
103. P. Ewels, M. Magnusson, S. Lundin, M. Käller, MultiQC: Summarize analysis results for multiple tools and samples in a single report. *Bioinformatics* **32**, 3047–3048 (2016).
104. N. L. Bray, H. Pimentel, P. Melsted, L. Pachter, Near-optimal probabilistic RNA-seq quantification. *Nat. Biotechnol.* **34**, 525–527 (2016).
105. J. M. Mudge, S. Carbonell-Sala, M. Diekhans, J. G. Martinez, T. Hunt, I. Jungreis, J. E. Loveland, C. Arnan, I. Barnes, R. Bennett, A. Berry, A. Bignell, D. Cerdán-Vélez, K. Cochran, L. T. Cortés, C. Davidson, S. Donaldson, C. Dursun, R. Fatima, M. Hardy, P. Hebbar, Z. Hollis, B. T. James, Y. Jiang, R. Johnson, G. Kaur, M. Kay, R. J. Mangan, M. Maquedano, L. M. Gómez, N. Mathlouthi, R. Merritt, P. Ni, E. Palumbo, T. Perteghella, F. Pozo, S. Raj, C. Sisu, E. Steed, D. Sumathipala, M.-M. Suner, B. Uszczynska-Ratajczak, E. Wass, Y. T. Yang, D. Zhang, R. D. Finn, M. Gerstein, R. Guigó, T. J. P. Hubbard, M. Kellis, A. Kundaje, B. Paten, M. L. Tress, E. Birney, F. J. Martin, A. Frankish, GENCODE 2025: Reference gene annotation for human and mouse. *Nucleic Acids Res.* **53**, D966–D975 (2025).
106. V. A. Schneider, T. Graves-Lindsay, K. Howe, N. Bouk, H. C. Chen, P. A. Kitts, T. D. Murphy, K. D. Pruitt, F. Thibaud-Nissen, D. Albracht, R. S. Fulton, M. Kremitzki, V. Magrini, C. Markovic, S. McGrath, K. M. Steinberg, K. Auger, W. Chow, J. Collins, G. Harden, T. Hubbard, S. Pelan, J. T. Simpson, G. Threadgold, J. Torrance, J. M. Wood, L. Clarke, S. Koren, M. Boitano, P. Peluso, H. Li, C. S. Chin, A. M. Phillippy, R. Durbin, R. K. Wilson, P. Flicek, E. E. Eichler, D. M. Church, Evaluation of GRCh38 and de novo haploid genome assemblies demonstrates the enduring quality of the reference assembly. *Genome Res.* **27**, 849–864 (2017).
107. C. Soneson, M. I. Love, M. D. Robinson, Differential analyses for RNA-seq: Transcript-level estimates improve gene-level inferences. *F1000Res* **4**, 1521 (2015).
108. M. I. Love, W. Huber, S. Anders, Moderated estimation of fold change and dispersion for RNA-seq data with DESeq2. *Genome Biol.* **15**, 550 (2014).
109. The Gene Ontology Consortium, S. A. Aleksander, J. Balhoff, S. Carbon, J. M. Cherry, H. J. Drabkin, D. Ebert, M. Feuermann, P. Gaudet, N. L. Harris, D. P. Hill, R. Lee, H. Mi, S. Moxon, C. J. Mungall, A. Muruganugan, T. Mushayahama, P. W. Sternberg, P. D. Thomas, K. Van Auken, J. Ramsey, D. A. Siegele, R. L. Chisholm, P. Fey, M. C. Aspromonte, M. V. Nugnes, F. Quaglia, S. Tosatto, M. Giglio, S. Nadendla, G. Antonazzo, H. Attrill, G. Dos Santos, S. Marygold, V. Strelets, C. J. Tabone, J. Thurmond, P. Zhou, S. H. Ahmed, P. Asanitthong, D. Luna Buitrago, M. N. Erdol, M. C. Gage, M. Ali Kadhum, K. Y. C. Li, M. Long, A. Michalak, A. Pesala, A. Pritazahra, S. C. C. Saverimuttu, R. Su, K. E. Thurlow, R. C. Lovering, C. Logie, S. Oliferenko, J. Blake, K. Christie, L. Corbani, M. E. Dolan, H. J. Drabkin, D. P. Hill, L. Ni, D. Sitnikov, C. Smith, A. Cuzick, J. Seager, L. Cooper, J. Elser, P. Jaiswal, P. Gupta, P. Jaiswal, S. Naithani, M. Lera-Ramirez, K. Rutherford, V. Wood, J. L. De Pons, M. R. Dwinell, G. T. Hayman, M. L. Kaldunski, A. E. Kwitek, S. J. F. Laulederkind, M. A. Tutaj, M. Vedi, S.-J. Wang, P. D'Eustachio, L. Aimo, K. Axelsen, A. Bridge, N. Hyka-Nouspikel, A. Morgat, S. A. Aleksander, J. M. Cherry, S. R. Engel, K. Karra, S. R. Miyasato, R. S. Nash, M. S. Skrzypek, S. Weng, E. D. Wong, E. Bakker, T. Z. Berardini, L. Reiser, A. Auchincloss, K. Axelsen, G. Argoud-Puy, M.-C. Blatter, E. Boutet, L. Breuza, A. Bridge, C. Casals-Casas, E. Coudert, A. Estreicher, M. Livia Famiglietti, M. Feuermann, A. Gos, N. Gruaz-Gumowski, C. Hulo, N. Hyka-Nouspikel, F. Jungo, P. Le Mercier, D. Lieberherr, P. Masson, A. Morgat, I. Pedruzzi, L. Pourcel, S. Poux, C. Rivoire, S. Sundaram, A. Bateman, E. Bowler-Barnett, H. Bye-A-Jee, P. Denny, A. Ignatchenko, R. Ishtiaq, A. Lock, Y. Lussi, M. Magrane, M. J. Martin, S. Orchard, P. Raposo, E. Speretta, N. Tyagi, K. Warner, R. Zaru, A. D. Diehl, R. Lee, J. Chan, S. Diamantakis, D. Raciti, M. Zarowiecki, M. Fisher, C. James-Zorn, V. Ponferrada, A. Zorn, S. Ramachandran, L. Ruzicka, M. Westerfield, The Gene Ontology knowledgebase in 2023. *Genetics* **224**, iyad031 (2023).
110. S. X. Ge, D. Jung, R. Yao, ShinyGO: A graphical gene-set enrichment tool for animals and plants. *Bioinformatics* **36**, 2628–2629 (2020).
111. F. Supek, M. Bošnjak, N. Škunca, T. Šmuc, REVIGO summarizes and visualizes long lists of Gene Ontology terms. *PLOS ONE* **6**, e21800 (2011).
112. P. Shannon, A. Markiel, O. Ozier, N. S. Baliga, J. T. Wang, D. Ramage, N. Amin, B. Schwikowski, T. Ideker, Cytoscape: A software environment for integrated models of biomolecular interaction networks. *Genome Res.* **13**, 2498–2504 (2003).

Downloaded from https://www.science.org on October 19, 2025

113. N. T. Doncheva, J. H. Morris, H. Holze, R. Kirsch, K. C. Nastou, Y. Cuesta-Astroz, T. Rattei, D. Szklarczyk, C. von Mering, L. J. Jensen, Cytoscape stringApp 2.0: Analysis and visualization of heterogeneous biological networks. *J. Proteome Res.* **22**, 637–646 (2023).
114. D. Szklarczyk, R. Kirsch, M. Koutrouli, K. Nastou, F. Mehryary, R. Hachilif, A. L. Gable, T. Fang, N. T. Doncheva, S. Pyysalo, P. Bork, L. J. Jensen, C. von Mering, The STRING database in 2023: Protein-protein association networks and functional enrichment analyses for any sequenced genome of interest. *Nucleic Acids Res.* **51**, D638–D646 (2023).
115. Y. Hao, T. Stuart, M. H. Kowalski, S. Choudhary, P. Hoffman, A. Hartman, A. Srivastava, G. Molla, S. Madad, C. Fernandez-Granda, R. Satija, Dictionary learning for integrative, multimodal and scalable single-cell analysis. *Nat. Biotechnol.* **42**, 293–304 (2024).
116. P. L. Germain, A. Lun, C. Garcia Meixide, W. Macnair, M. D. Robinson, Doublet identification in single-cell sequencing data using *scDblFinder*. *F1000Res* **10**, 979 (2021).
117. T. Wu, E. Hu, S. Xu, M. Chen, P. Guo, Z. Dai, T. Feng, L. Zhou, W. Tang, L. Zhan, X. Fu, S. Liu, X. Bo, G., clusterProfiler 4.0: A universal enrichment tool for interpreting omics data. *Innovation* **2**, 100141 (2021).
118. J. T. Robinson, H. Thorvaldsdóttir, W. Winckler, M. Guttman, E. S. Lander, G. Getz, J. P. Mesirov, Integrative genomics viewer. *Nat. Biotechnol.* **29**, 24–26 (2011).

Acknowledgments: We would like to thank the South African Heritage Resources Agency (SAHRA), B. Zipfel from the Evolutionary Studies Institute of the University of Witwatersrand, and M. Tawane from the Ditsong National Museum of Natural History for granting the export permit of the valuable samples for analyses. We want to thank C. Lawrence and K. Simon-Menasse from Perth Zoo, who provided access to modern orangutan dental material. We also want to thank W. Pontes for the administrative support. We acknowledge the support of K. Jepsen at the UCSD Institute of Genomic Medicine. We would like to thank Southern Cross University for the PhD scholarship support of M.B. The AI-based tool Grammarly (version 9.75.0) was used solely to check grammar, spelling, and general readability of the manuscript. ChatGPT-4 (GPT-4-turbo), developed by OpenAI, version dated December 2024, was used to assist in the curation and structuring of GO:BP terms. The full details of the use can be found in the "Use of AI for GO term curation" section, and all prompts are available in Zenodo and GitHub (https://zenodo.org/records/16628925 and https://github.com/galantelab/jb_2025_SAdv). The Payre excavations were supported by the French Ministry of Culture, Service régional de l'archéologie, Auvergne-Rhône-Alpes. **Funding:** This work was supported by the UCSD Archaealization Center (ArchC), the Neanderthal Brain Foundation, and the National Institutes of Health (NIH R01MH100175) (A.R.M.) and the California Institute for Regenerative Medicine (CIRM DISC4-16377) (A.R.M.). We acknowledge K. Jepsen at the UCSD Institute of Genomic Medicine funded by the National Institutes of Health (NIH S10 OD026929) and the US National Institute of Environmental Health Sciences (NIEHS R01ES027981) (B.L.); Pontifícia Universidade Católica do Paraná (PUCPR, Curitiba, Brazil) (R.H.H. and L.P.P.); the Australian Research Council Discovery Grants (DP170101597 and DP220100195) and LIEF Grant (LE200100022) (R.J.-B.); ARC Discovery Grant (DP230100440) (K.W.); ARC Future Fellowship (#FT220100184) (I.M.); the US National Institute of Environmental Health Sciences (P30ES023515, R01ES026033, U2CES030859, U2CES026561, R35ES030435, and UL1TR004419) (M.A.); Monash Interdisciplinary Research Seed Funding Scheme 2019 (L.F., J.W.A., and R.J.-B.); the National Council for Scientific and Technological Development (CNPq grants 311438/2022-9 and 402773/2022-5) (R.H.H.); the National Science Foundation (NSF BCS 0962564) and the Leakey Foundation (J.W.A.); Coordenação de Aperfeiçoamento de Pessoal de Nível Superior (L.P.P.); São Paulo Research Foundation [FAPESP grants 2018/15579-8 (P.A.F.G.), 2023/07144-0 and #2020/14158-9 (F.F.d.S.), and 2020/02413-4 (R.L.V.M.)]; and the Young Scientist Program at Hospital Sírio-Libanês (G.D.A.G.). **Author contributions:** Conceptualization: R.J.-B., J.S.d.S., A.R.M., M.A., B.L., J.W.A., W.W., P.A.F.G., and K.W. Methodology: R.J.-B., J.S.d.S., A.R.M., M.A., B.L., J.W.A., P.A.F.G., C.A., A.M.A.M., R.H.H., S.M.S.-S., B.L.T., J.Y., and C.A.B. Software: R.J.-B., R.H.H., F.F.d.S., G.D.A.G., J.Y., and R.L.V.M. Validation: R.J.-B., J.S.d.S., A.R.M., M.A., W.W., P.A.F.G., R.H.H., F.F.d.S., Y.Z., G.T.S., L.P.P., S.M.S.-S., B.L.T., and M.-H.M. Formal analysis: R.J.-B., J.S.d.S., A.R.M., M.A., B.L., J.W.A., C.A., A.M.A.M., R.H.H., F.F.d.S., G.D.A.G., L.P.P., R.L.V.M., and F.D. Investigation: R.J.-B., J.S.d.S., A.R.M., M.A., B.L., M.B., J.W.A., W.W., C.A., A.M.A.M., R.H.H., I.M., G.T.S., S.M.S.-S., B.L.T., C.A.B., M.-H.M., F.D., and M.T. Resources: R.J.-B., J.S.d.S., A.R.M., M.A., J.W.A., W.W., P.A.F.G., L.F., A.M.A.M., Y.Z., B.L.T., J.Y., and M.-H.M. Data curation: R.J.-B., J.S.d.S., A.R.M., M.A., B.L., P.A.F.G., L.F., A.M.A.M., R.H.H., F.F.d.S., G.T.S., L.P.P., J.O., M.-H.M., and R.L.V.M. Writing—original draft: R.J.-B., J.S.d.S., A.R.M., M.A., J.W.A., C.A., G.T.S., and S.M.S.-S. Writing—review and editing: R.J.-B., J.S.d.S., A.R.M., M.A., B.L., J.W.A., P.A.F.G., C.A., L.F., A.M.A.M., R.H.H., F.F.d.S., G.D.A.G., Y.Z., I.M., G.T.S., L.P.P., S.M.S.-S., B.L.T., J.Y., C.A.B., W.L., M.T., and K.W. Visualization: R.J.-B., J.S.d.S., A.R.M., M.A., B.L., A.M.A.M., R.H.H., F.F.d.S., G.D.A.G., I.M., L.P.P., J.O., R.L.V.M., and F.D. Supervision: R.J.-B., A.R.M., M.A., B.L., P.A.F.G., Y.Z., I.M., and J.Y. Project administration: R.J.-B., J.S.d.S., A.R.M., M.A., J.W.A., J.Y., and M.-H.M. Funding acquisition: R.J.-B., A.R.M., M.A., B.L., J.W.A., L.F., J.Y., C.A.B., M.-H.M., and K.W. **Competing interests:** A.R.M. is the cofounder of and has an equity interest in TISMOO, a company dedicated to genetic analysis and human brain organogenesis, focusing on therapeutic applications customized to autism spectrum disorders and other neurological diseases. A.R.M. has several patents on stem cells and brain organoid models. The terms of this arrangement have been reviewed and approved by the University of California, San Diego in accordance with its conflict-of-interest policies. C.A. and M.A. are founders of Linus Biotechnology Inc. The terms of this arrangement have been reviewed and approved by the Mount Sinai Health System in accordance with its conflict-of-interest policies. The company was not involved with any component of this study. Other authors declare that they have no competing interests. B.L.T. and C.A.B. were used by NGeneBioAI, a for-profit entity, at the time of their contribution to this work. **Data and materials availability:** All sequencing data (scRNA-seq and bulk RNA-seq) are available under European Nucleotide Archive accession code ENA PRJEB83863. All other data needed to evaluate the conclusions in the paper are present in the paper and/or the Supplementary Materials. All scripts used to process and analyze these data are available in the GitHub repository (https://github.com/galantelab/jb_2025_SAdv) and in Zenodo repository (https://zenodo.org/records/16628925). All fossil materials were returned to their respective museums and repository collections (China: IVVP Beijing and Shandong University Museum collections; South Africa: Ditsong Museum and the University of Witwatersrand repository collection; France: Museum National d'Histoire Naturelle in Paris; Indonesia: Centre for Archaeology in Padang Sumatra and the National Research and Innovation Agency BRIN—Badan Riset dan Inovasi Nasional—in Jakarta) and can be accessed upon request and approval by the relevant authorities. The modern human teeth (USA; table S1) analyzed in this study are part of ongoing research at the Mount Sinai School of Medicine, while the modern *Pongo* samples from Perth Zoo (Australia; table S1) are curated at Southern Cross University. Both collections are available upon request from their respective institutions, subject to the necessary clearances. The MS proteomics data have been deposited to the ProteomeXchange Consortium via the PRIDE partner repository with the dataset identifier PXD067623.

Submitted 17 June 2024
Accepted 2 September 2025
Published 15 October 2025
10.1126/sciadv.adr1524

Downloaded from https://www.science.org on October 19, 2025